Simulation of Seasonal Variation of Marine Boundary Layer Clouds over the Eastern Pacific with a Regional Climate Model*

LEI WANG, YUQING WANG, AXEL LAUER, AND SHANG-PING XIE

International Pacific Research Center, School of Ocean and Earth Science and Technology, University of Hawaii at Manoa, Honolulu, Hawaii

(Manuscript received 8 July 2010, in final form 25 November 2010)

ABSTRACT

The seasonal cycle of marine boundary layer (MBL) clouds over the eastern Pacific Ocean is studied with the International Pacific Research Center (IPRC) Regional Atmospheric Model (iRAM). The results show that the model is capable of simulating not only the overall seasonal cycle but also the spatial distribution, cloud regime transition, and vertical structure of MBL clouds over the eastern Pacific. Although the modeled MBL cloud layer is generally too high in altitude over the open ocean when compared with available satellite observations, the model simulated well the westward deepening and decoupling of the MBL, the rise in cloud base and cloud top of the low cloud decks off the Peru and California coasts, and the cloud regime transition from stratocumulus near the coast to trade cumulus farther to the west in both the southeast and northeast Pacific. In particular, the model reproduced major features of the seasonal variations in stratocumulus decks off the Peru and California coasts, including cloud amount, surface latent heat flux, subcloud-layer mixing, and the degree of MBL decoupling. In both observations and the model simulation, in the season with small low-level cloudiness, surface latent heat flux is large and the cloud base is high. This coincides with weak subcloud-layer mixing and strong entrainment at cloud top, characterized by a high degree of MBL decoupling, while the opposite is true for the season with large low-level cloudiness. This seasonal cycle in low-cloud properties resembles the downstream stratocumulus-to-cumulus transition of marine low clouds and can be explained by the ''deepening–decoupling'' mechanism proposed in previous studies. It is found that the seasonal variations of low-level clouds off the Peru coast are mainly caused by a large seasonal variability in sea surface temperature, whereas those off the California coast are largely attributed to the seasonal cycle in lower-tropospheric temperature.

1. Introduction

Marine boundary layer (MBL) clouds off the west coasts of the continents have a great impact on climate because of their significant effect on the global radiation budget (Hartmann et al. 1992). Understanding relevant mechanisms responsible for the maintenance and variabilities of these clouds is therefore crucial for climate research (Randall et al. 1984). Spectral analysis of MBL cloud time series reveals that most of the variability occurs on seasonal-to-interannual time scales (Rozendaal and Rossow 2003). The seasonal cycle of global low-level stratiform clouds was studied by Klein and Hartmann (1993) using surface-based observations. They showed a very high correlation between monthly-mean low-level cloud amount and lower-tropospheric stability (LTS). Rozendaal and Rossow (2003) extended the analysis of the seasonal variations to include variations of cloud-top pressure and cloud optical thickness based on satellite products.

Lin et al. (2009) investigated the seasonal variation of physical properties of low-level clouds, including cloud amount, cloud-top and cloud-base heights, degree of decoupling, and inversion strength off the California coast using multisatellite observations. They indicated that the seasonal variation of low-level cloud properties off the California coast resembles the downstream stratocumulus-to-cumulus transition extensively studied previously (e.g., Wyant et al. 1997; Bretherton and Wyant 1997). A similar

* International Pacific Research Center Publication Number 775 and School of Ocean and Earth Science and Technology Publication Number 8130.

Corresponding author address: Dr. Yuqing Wang, IPRC, SOEST, University of Hawaii at Manoa, 1680 East-West Road, Honolulu, HI 96822.
E-mail: yuqing@hawaii.edu

DOI: 10.1175/2010JCLI3935.1

analogy was drawn for cloud variations in the southeast Pacific based on a coupled model simulation (Xie et al. 2007). Namely, the deepening of the MBL associated with large cloud-top entrainment can lead to reduced vertical mixing in the subcloud layer and a high degree of decoupling of the MBL. This would promote trade cumulus clouds, which entrain significant amounts of dry air from above the inversion, resulting in evaporation and thinning of the stratocumulus clouds and a significant reduction of low-cloud fraction.

Despite their climatic importance, MBL clouds have proven difficult to simulate in climate models (Bretherton et al. 2004b) because they are only a few hundred meters thick, capped by a sharp temperature inversion and maintained by various physical processes, including complex interactions among the atmosphere, ocean, and land. Simulation of MBL clouds in global climate models (GCMs) is among the most problematic, and few models can simulate the extent of MBL clouds and their albedo realistically (Ma et al. 1996; Siebesma et al. 2004; Bender et al. 2006; Lin 2007; de Szoeke and Xie 2008; Wyant et al. 2010). Sensitivity of MBL clouds to changes in environmental conditions has been identified as a major source of uncertainty in tropical and subtropical cloud feedbacks in current GCMs (Bony and Dufresne 2005) and as a primary source of uncertainty in climate sensitivity as documented in the Intergovernmental Panel on Climate Change (IPCC) Fourth Assessment Report (Randall et al. 2007). Comparisons of results from 10 atmospheric GCMs with satellite measurements show that the simulated seasonal variations of low-level clouds are generally poor compared with those of high-level clouds (Zhang et al. 2005). Because of the crucial effect of MBL clouds on the earth's energy budget, an improved representation of these clouds in climate models is of particular importance for climate change studies.

Several studies using regional atmospheric models show significant improvements in simulating MBL clouds over the eastern Pacific (McCaa and Bretherton 2004; Bretherton et al. 2004a; Wang et al. 2004a,b; Lauer et al. 2009). Although some global climate models are increasing their resolutions and use physics parameterizations with a level of complexity comparable to regional climate models, running high-resolution regional models is still attractive because they are computationally not very expensive and can help to study areas of particular interest. Here, we use the latest version of the International Pacific Research Center (IPRC) Regional Atmospheric Model (iRAM) to study MBL clouds over the eastern Pacific. The iRAM has been shown skillful in simulating the stratocumulus deck, the cloud regime transition, and vertical cloud structure over the southeastern Pacific (Wang et al. 2004a,b; Lauer et al. 2009). Lauer et al. (2009) implemented a double-moment cloud microphysics scheme (Phillips et al. 2007, 2008, 2009) into the iRAM and compared the simulation extensively with available observations. They showed that the model is able to simulate mean cloud properties, such as liquid water content, cloud droplet number concentration, cloud cover, and cloud radiative forcing, reasonably well during August–October 2006. The diurnal cycle of cloud liquid water over the eastern Pacific is also reasonably simulated by the iRAM, which is shown in Wang et al. (2004a) and Lauer et al. (2009). Recently, Lauer et al. (2010) show that the iRAM has considerable skills in simulating not only climatological mean properties of MBL clouds but also interannual cloud variations in the eastern Pacific, and they apply the model to assess the potential impact of global warming on MBL clouds in this region.

In this study, we extend previous studies to examine the seasonal variations of MBL clouds simulated by the iRAM and compare the model results with available observations, particularly satellite measurements. We have two main objectives: (i) to evaluate the model's capability in reproducing the observed seasonal cycle of MBL clouds over the eastern Pacific and (ii) to understand the physical processes involved. The regional climate model iRAM and the model setup are described in section 2. Simulation results and comparisons with observations are presented in section 3. In section 4, we discuss the mechanism of the seasonal cycle of MBL clouds over the eastern Pacific. A summary and conclusions are given in the last section.

2. Model, experiment, and observational datasets

a. *Model*

In this work the iRAM is used to study the seasonal variation of MBL clouds over the eastern Pacific. The iRAM is based on the hydrostatic primitive equations in σ coordinates (Wang et al. 2003, 2004a). Cloud microphysics are calculated by a double-moment cloud microphysics scheme with a prognostic treatment of six aerosol species inside clouds (Phillips et al. 2007, 2008, 2009), which replaces the original single-moment cloud microphysics module of Wang (2001). The cloud microphysics module is coupled to the radiation scheme and provides effective radii of cloud droplets and ice crystals as well as the liquid water and ice contents as inputs for the radiative transfer calculations. The radiation scheme is based on the radiation package of Edwards and Slingo (1996) with improvements by Sun and Rikus (1999). It consists of four bands in the solar spectral range and seven bands in the thermal spectral range. Subgrid-scale convection, including shallow, midlevel, and deep convection, is parameterized following Tiedtke (1989) with modifications by Gregory et al. (2000). Cloud amount is diagnosed from cloud liquid water/ice content and relative humidity following Xu and Randall (1996). For more details on the iRAM, refer to Wang (2001), Wang et al. (2003, 2004a), and the literature cited therein. Additional details on the double-moment cloud microphysics scheme and a model evaluation can be found in Phillips et al. (2007, 2008, 2009) and Lauer et al. (2009), respectively.

b. Experiment

The experiment performed in this study uses the model domain covering the tropical and subtropical eastern Pacific (40°S–40°N, 160°–50°W) with a horizontal resolution of 0.5° longitude $\times$ 0.5° latitude. There are 28 vertical levels from the surface up to about 10 hPa with 11 layers below 800 hPa. The boundary conditions for the model integration are obtained from the National Centers for Environmental Prediction (NCEP) final (FNL) analysis with a horizontal resolution of 1° $\times$ 1° and 26 vertical pressure levels at 6-h time intervals after year 2000, which are interpolated to the model grid and time.[1] [Dataset ds083.2, published by the Computational Information Systems Laboratory (CISL) data support section at the National Center for Atmospheric Research (NCAR), is available online at dss.ucar.edu/datasets/ds083.2/.] NCEP–NCAR reanalysis data with a horizontal resolution of 2.5° $\times$ 2.5° and 17 pressure levels at 6-h intervals are used as initial as well as lateral boundary conditions prior to the year 2000 (Kalnay et al. 1996). Sea surface temperatures (SSTs) are prescribed according to the National Oceanic and Atmospheric Administration (NOAA) analyses (Reynolds et al. 2007) based on daily mean satellite observations from the Advanced Very High Resolution Radiometer (AVHRR) and the Advanced Microwave Scanning Radiometer (AMSR). The prognostic model variables are nudged to the NCEP FNL analysis (or NCEP–NCAR reanalysis) data within a 10° buffer zone along the lateral boundaries. We performed a 12-yr continuous simulation from January 1997 through December 2008. Unless otherwise noted, all seasonal cycles of MBL cloud properties discussed in the following sections are calculated by averaging model data and observations over the entire 12-yr period.

[1] The U.S. National Centers for Environmental Prediction updates daily the NCEP FNL Operational Model Global Tropospheric Analyses, continuing from July 1999.

c. Observational datasets

In addition to the NCEP FNL analysis, the NCEP–NCAR reanalysis, and the AMSR SST, more data are used for verification of the model simulation discussed in the next section. Simulation of surface winds is compared with the seasonal means of Quick Scatterometer (QuikSCAT) measurements over the ocean for the period from July 1999 through December 2008. The SeaWinds scatterometer on board the QuikSCAT satellite is a microwave radar launched and operated by the National Aeronautics and Space Administration (NASA), which has provided measurements of near-surface winds over the world's oceans since July 1999. We use monthly-mean QuikSCAT data at 25-km resolution provided by Remote Sensing Systems (www.ssmi.com/qscat/qscat_browse.html).

Column water vapor from the Special Sensor Microwave Imager (SSM/I) is used for comparison, which is a passive radiometer measuring the thermal emissions of the earth and the atmosphere. Here, we use the monthly-mean SSM/I data at a resolution of 25 km provided by Remote Sensing Systems (www.ssmi.com/ssmi/ssmi_browse.html). The observations of the seasonal mean liquid water path (LWP) are taken from the University of Wisconsin (UWisc) climatology derived from SSM/I, Tropical Rainfall Measuring Mission Microwave Imager (TMI), and AMSR for Earth Observing System (AMSR-E) passive microwave observations over the oceans (O'Dell et al. 2008).

The low-level cloud amount is obtained from the International Satellite Cloud Climatology Project (ISCCP) D2 product (Rossow et al. 1996; Rossow and Schiffer 1999). The satellite data are monthly means on a 2.5° $\times$ 2.5° grid starting from July 1983. Low clouds in ISCCP are referred to clouds with tops below 680 hPa. Following Clement et al. (2009), we use low-plus-midlevel cloud amounts from ISCCP rather than low-level cloud amount only because low-level cloud amount L can be mistakenly identified as midlevel cloud amount U, particularly in the southeast Pacific. We calculated a corrected low-level cloud amount L' based on $L' = L/(1 - U)$, after Rozendaal et al. (1995) and Mansbach and Norris (2007).

The simulated low-level cloud-base and cloud-top heights are compared with the cloud-layer product from Cloud–Aerosol Lidar and Infrared Pathfinder Satellite Observations (CALIPSO). CALIPSO was launched on 28 April 2006 and is a two-wavelength (532 and 1064 nm) lidar providing high-resolution vertical profiles of aerosols and clouds. Details on CALIPSO and the algorithms used can be found in Winker et al. (2009). Boundary layer clouds are detected at a resolution of 30 m in the vertical and 333 m in the horizontal. The full-resolution product

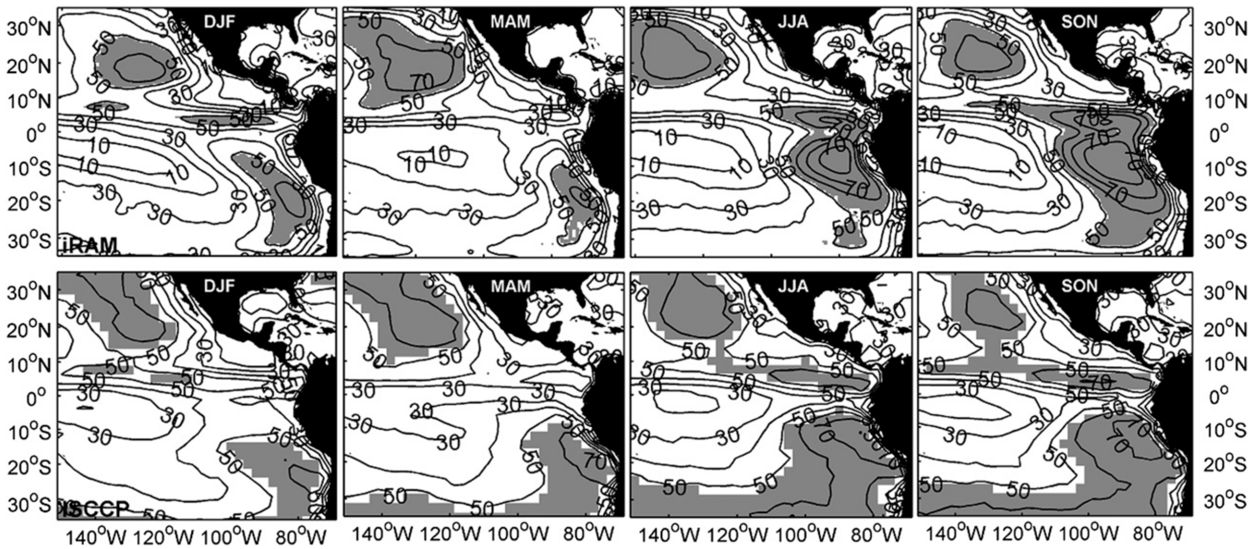

FIG. 1. Seasonal mean low-level cloud fraction (contours in %): (top) iRAM simulation and (bottom) ISCCP satellite observations. Regions with low-cloud fractions greater than 50% are shaded.

provides up to five cloud layers per profile, as provided by the NASA Langley Atmospheric Science Data Center (ASDC) (http://eosweb.larc.nasa.gov/). The maximum cloud-top height of the first cloud layer is below 3000 m and is considered to represent low-level clouds in this study. All available cloud-base and cloud-top height data for low-level clouds starting from June 2006 are averaged to calculate seasonal means within each 2.5° × 2.5° grid cell.

The shortwave and longwave cloud-radiative forcing at the top of the atmosphere (TOA) was obtained from the Clouds and the Earth's Radiant Energy System (CERES) satellite observations. As in Lauer et al. (2009), we used the CERES FM1 + FM3 Edition 2 ES4 dataset (Wielicki et al. 1996; http://eosweb.larc.nasa.gov/PRODOCS/ceres/table_ceres.html). We calculate the shortwave cloud forcing (SCF) [longwave cloud forcing (LCF)] at TOA as the difference between the all-sky shortwave (longwave) radiation flux and the clear-sky shortwave (longwave) radiation flux at the TOA. The ES4 dataset used here provides monthly means at a spatial resolution of 2.5° × 2.5°. It covers the time period from July 2002 through December 2008.

The objective analyzed air–sea fluxes (OAFlux) dataset (Yu and Weller 2007; http://oaflux.whoi.edu/) is used as a reference for the simulated surface fluxes. The OAFlux products are calculated from basic surface meteorological variables obtained from a variational objective analysis using bulk flux algorithms. Several data sources were synthesized in the objective analysis, including the SSM/I and AVHRR satellites as well as the European Centre for Medium-Range Weather Forecasts (ECMWF) and the NCEP–U.S. Department of Energy Global Reanalysis 2 (NCEP-2).

3. Results

In this section, we will first verify the simulated cloud properties, including low-level cloud amount, liquid water path, cloud-base and cloud-top heights, cloud thickness, and the vertical structure of low clouds, against available observations. We will then compare the simulated dynamical variables with observations and discuss physical processes related to the seasonal variation of observed and simulated low clouds over both the Peruvian stratocumulus region (25°–5°S, 100°–75°W) and the California stratocumulus region (15°–30°N, 140°–120°W).

a. Cloud properties

1) Low-level cloud amount

Figure 1 compares the simulated seasonal and ISCCP mean low-level cloud amounts. The satellite observations show three regions of large low-cloud cover with average values exceeding 50% near the intertropical convergence zone (ITCZ) between 3° and 10°N and over the two stratocumulus decks off the Peru and California coasts. They all show a distinct seasonal cycle, particularly the two stratocumulus decks. For the Peruvian region, the low-cloud fraction shows high average values exceeding 60% in September–November (SON) and June–August (JJA), and low average values below 45% in March–May (MAM) and December–February (DJF). In the California region, high low-cloud fraction with average values exceeding 55% is present in JJA and

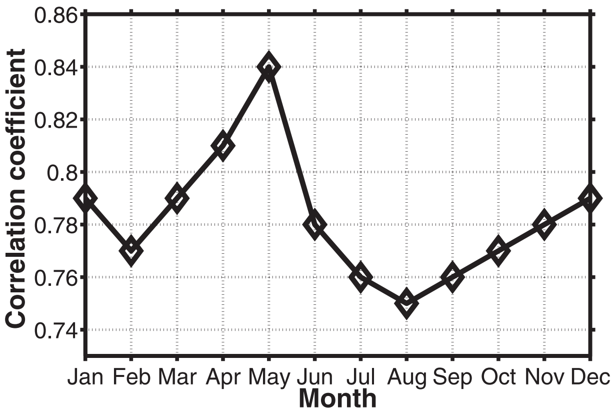

FIG. 2. Spatial correlation coefficients for multiyear monthly-mean low-level cloudiness between iRAM simulation and ISCCP observations averaged over the region 35°S–35°N, 150°–70°W.

MAM, and low low-cloud fraction with average values below 50% is found in DJF and SON. Both the geographic distribution and seasonal variation of the low-level cloud fraction are simulated by the iRAM reasonably well. In particular, the model reproduces the distinct decrease in low-level cloud fraction farther westward off the continents over the subtropical Pacific in both hemispheres. This rapid decrease in low-level cloudiness is associated with a transition from stratocumulus clouds to trade cumuli resulting from the increase in SST (see discussion in section 3b).

The linear spatial correlation coefficients between the modeled and the ISCCP observed monthly-mean low-cloud fractions are more than 75% year round, reaching 84% in May (Fig. 2). The spatial correlation coefficients between the modeled and observed seasonal mean low-cloud fractions vary between 77% and 81% and that the annual mean is 79% (not shown). The high spatial correlation between the simulation and observation demonstrates that the model has considerable skill in reproducing not only the spatial distribution but also the seasonal cycle of the observed low clouds in the eastern Pacific. Note that the position of the modeled stratocumulus deck is shifted by about 8° to the northwest over the southeast Pacific and by 9° to the west over the northeast Pacific compared with observations. The modeled low-level cloud fraction in the southwest quarter of the domain is consistently lower than ISCCP observations by 10%–20%. These model biases could be partly because the model horizontal resolution is not high enough to resolve realistically the high and steep Andes and the sharp land–sea contrast in the western coastal regions of both South and Central Americas (Wang et al. 2004a).

2) CLOUD LWP

Figure 3 shows a comparison of the seasonal mean LWP simulated in the iRAM with satellite observations (UWisc). The geographical pattern of LWP from observations shows high values in the ITCZ exceeding 180 g m^{-2} as well as in the two stratocumulus regions off the Peru and California coasts with average values of around 90 g m^{-2}. Regions with low LWP values (less than 40 g m^{-2}) are found between about 5° and 15°S and from 150° to about 100°W and over the eastern Pacific close to the coast of California. These features of the geographical LWP distribution are reproduced by the iRAM. However, the model does not reproduce the high

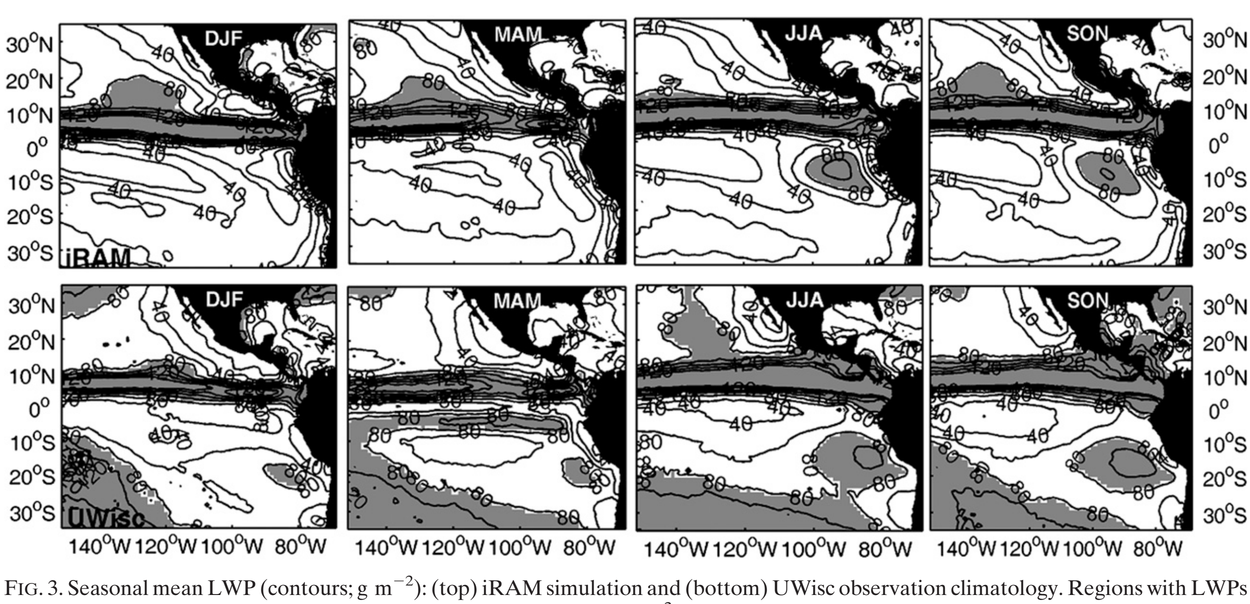

FIG. 3. Seasonal mean LWP (contours; g m^{-2}): (top) iRAM simulation and (bottom) UWisc observation climatology. Regions with LWPs greater than 80 g m^{-2} are shaded.

LWP values in MAM south of the equator between about 5°S and 10°S that are found in observations, which corresponds to a double ITCZ over the eastern Pacific during boreal spring, mainly in March and April (Zhang 2001). Although the double ITCZ in boreal spring was simulated well in the regional coupled ocean–atmosphere model (iROAM; Xie et al. 2007), which uses the same atmospheric model but with the bulk cloud microphysics scheme of Wang (2001), it does not show up in the latest uncoupled version of the iRAM, which uses a two-moment cloud microphysics scheme (see section 2a). A sensitivity run with the single-moment cloud microphysics scheme (Wang 2001) also does not reproduce the observed double ITCZ. This suggests that coupling with the ocean might be important for the formation of the double ITCZ in the eastern Pacific. This needs further analysis and diagnostics in a future study.

The seasonal variation of LWP over the Peruvian stratocumulus deck follows basically the seasonal variability of the low-level cloud fraction. For the California stratocumulus deck, the only exception is in SON, which shows higher values than in MAM, even though higher low-level cloudiness is found in MAM. This might be related to the differences in cloud thickness, which will be discussed in section 3b. The seasonal variation of LWP off the Peru coast is reproduced fairly well by the model, except for the northwest shift of modeled LWP, consistent with a similar shift in the low-level cloud fraction (Fig. 1). The iRAM underestimates the LWP peak in JJA in the California low-cloud region, which is mainly related to the underestimate of midlevel clouds in the region (not shown).

3) Low-level cloud-base and cloud-top heights, and cloud thickness

The simulated low-level cloud-base and cloud-top heights in the iRAM are compared with the cloud-layer product from CALIPSO in the Peruvian and California low-cloud regions in Figs. 4a and 4b, respectively. In the iRAM we define cloud-base height as the lowest level between surface and 3 km at which the daily mean cloud liquid water content exceeds 0.025 g kg^{-1} and cloud-top height as the highest level at which liquid water content falls below this threshold value. The daily mean cloud-base and cloud-top heights are then averaged to obtain the seasonal means using only model data after June 2006 to be consistent with the satellite observations.

Both cloud-base and cloud-top heights from CALIPSO observations increase gradually westward off the Peru and California coasts in all seasons. Off the Peru coast, the low-level cloud-base and cloud-top heights are the lowest in SON, with an average cloud base of 561 m and a cloud top of 1175 m, and they reach their maximum in MAM with an average cloud base of 995 m and a cloud top of 1607 m. Off the California coast, the low-level cloud-base and cloud-top heights are the lowest in JJA at 511 and 1105 m, respectively, and they reach their maximum in DJF at 839 and 1419 m, respectively. It is interesting to note that there is a close correlation between the seasonal variation of low-level cloud height and cloud amount. The season of the maximum low-level cloud amount corresponds to the season of the lowest low-level cloud-base and cloud-top heights (see Figs. 1 and 4).

The iRAM is capable of simulating the overall increase in cloud-base and cloud-top heights from the coast to open ocean and their seasonal variations in both stratocumulus regions in the southeast and northeast Pacific. The low-level cloud-base and cloud-top heights are, however, overestimated by 200–800 m over the open ocean about 1000 km off the coasts compared with CALIPSO observations. Previous modeling experiences using the iRAM reveal that the model generally fails to simulate the increase in cloud layer westward off the west coasts of Americas without the use of the shallow convection parameterization (see Wang et al. 2004b; de Szoeke et al. 2006). Comparing the present model results and the previous modeling results without the use of the shallow convection parameterization, the overestimations of the cloud heights in the present results might be because shallow convection parameterized in the model is too active. This overestimation was also shown in the simulation by the iRAM with single-moment cloud microphysics for the PreVOCA model comparison (Wyant et al. 2010).

The seasonal variation of the low cloud-base height roughly parallels that of the cloud-top height in the stratocumulus regions as can be seen from Fig. 4. As a result, the average cloud thickness (Fig. 5) remains at about 600 m and the seasonal variation in cloud thickness is relatively small ($<$100 m). The region with a cloud thickness of less than 400 m near the California coast is larger and extends farther westward in the model than in the CALIPSO observations. Because the overestimation of the cloud-top height is larger than that of cloud-base height, cloud thickness is generally overestimated in the model by 100–150 m over the open ocean about 1000 km off shore compared with CALIPSO observations, possibly due to too active shallow convection in the model as mentioned above.

To further examine the seasonal variation of the low cloud-layer height and thickness, we show in Fig. 6 the seasonal mean vertical cross-sections of liquid water content along 15°S and 25°N, respectively, from the iRAM.

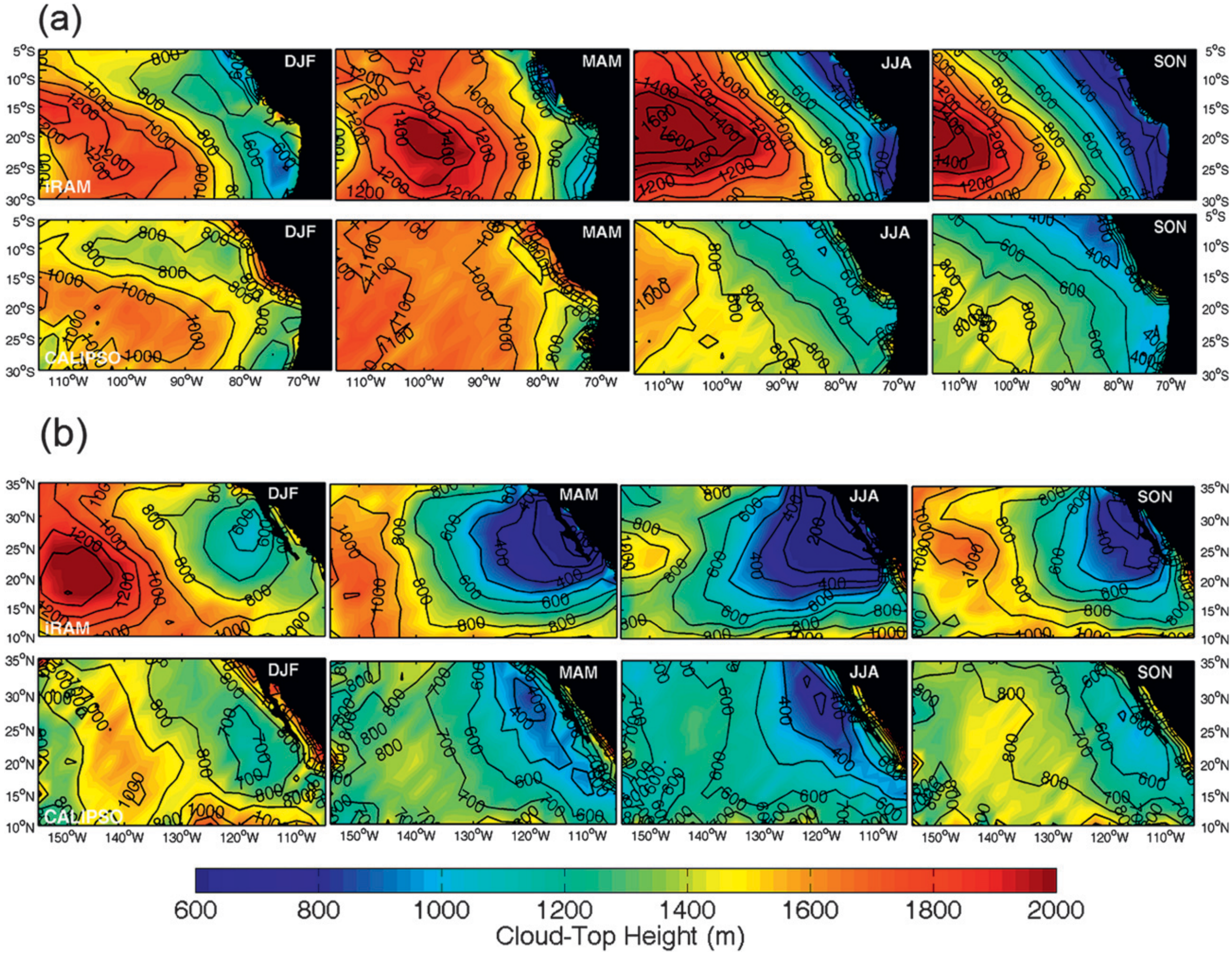

FIG. 4. Seasonal mean cloud-top height (shading; m) and cloud-base height (contours; m) in [top rows in (a),(b)] iRAM simulation and [bottom rows in (a),(b)] CALIPSO observations for the (a) Peru and (b) California coasts.

The boundary layer deepens westward in all seasons. Stratocumulus clouds are found close to the coasts and shallow trade cumulus convection with a deeper boundary layer is present farther to the west in the subtropics in both hemispheres. Off the Peruv coast (along 15°S), liquid water contents are higher in JJA and SON, concurrent with higher low-level cloud amounts in this region, than in DJF and MAM. Off the California coast (along 25°N), relatively low liquid water contents are present in DJF and SON and widely spread vertically in these two seasons in response to synoptic disturbances in boreal winter in the region (not shown) and the decoupling of the MBL (see discussion below). Higher liquid water contents occur in JJA and MAM, concurrent with the increased low-level cloud amounts in the region (Fig. 1). As already indicated above, the model cloud layer is generally too high in the western part of the model domain, possibly a result of too active shallow convection in the model.

4) CLOUD RADIATIVE FORCING

The shortwave (longwave) cloud radiative forcing quantifies the impact of clouds on the earth's radiation budget in the solar (thermal) spectral range. We calculate the SCF (LCF) at the TOA as the difference between the all-sky shortwave (longwave) radiation and the clear-sky shortwave (longwave) radiation at the TOA in the same way as for the satellite observation. Figure 7 shows a comparison of the seasonal mean SCF at the TOA simulated in the iRAM with CERES satellite observation. Both the geographical distribution and seasonal variation in SCF are consistent with the combined effect of the low-level cloud fraction and LWP in both the model and the observations. The model captures high absolute values along the ITCZ over the eastern Pacific but with an overestimation in most seasons. Observation shows the minimum SCF in DJF, while the model shows the minimum SCF in MAM in the ITCZ—a season later.

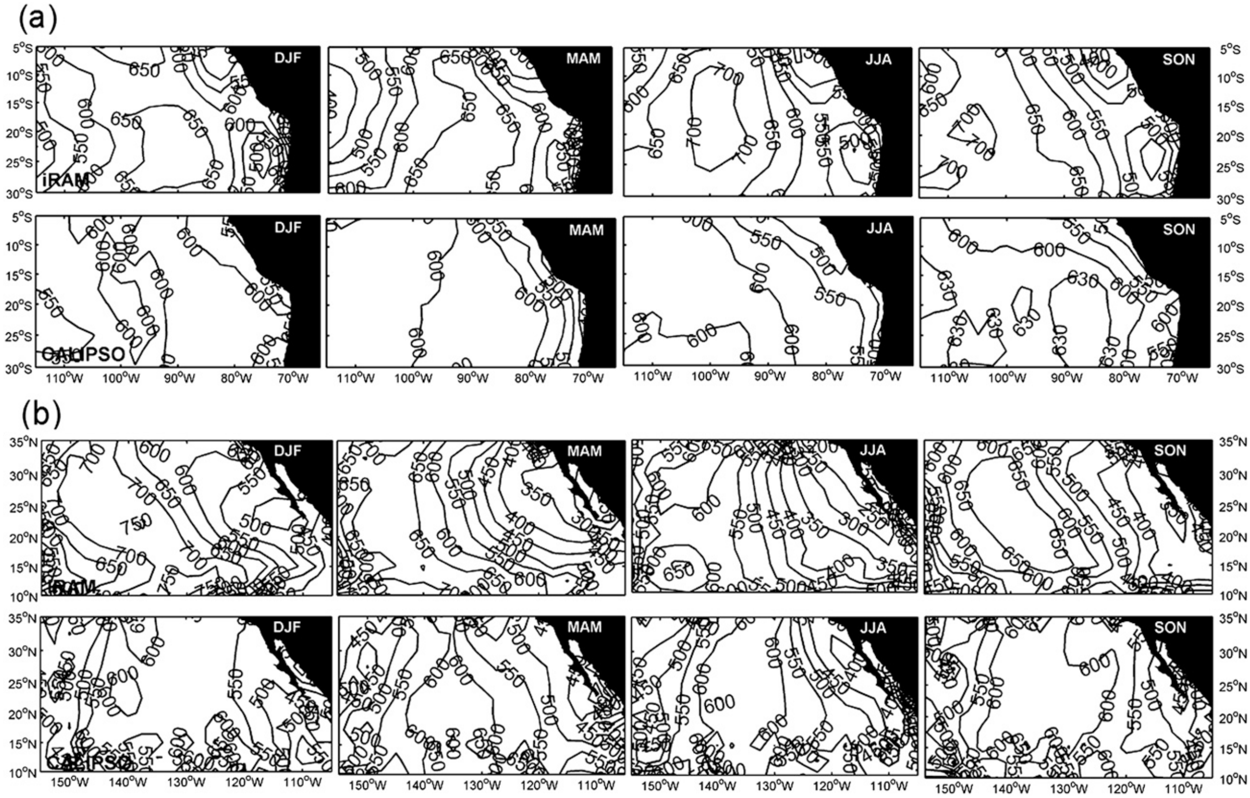

FIG. 5. Seasonal mean low-level cloud thickness (m) in [top rows in (a),(b)] iRAM simulation and [bottom rows in (a),(b)] CALIPSO observations for the (a) Peru and (b) California coasts.

The annual seasonal variation in SCF is underestimated in the model with an overestimation of the annual mean SCF by 20–30 W m^{-2} in the ITCZ, as found in the August–October mean in a simulation for 2006 in Lauer et al. (2009). The model simulated reasonably well the seasonal variation of SCF in the two stratocumulus regions off the Peru and California coasts, except for an overestimation of about 10–20 W m^{-2} in DJF and an underestimation of similar value in JJA, particularly in the coastal regions. Similar to that, in the ITCZ, the model displaces the observed minimum SCF from DJF to MAM and the maximum SCF from JJA to SON. The model also shows some bias in the southwest region of the model domain, with an underestimation in JJA and an overestimation in DJF and MAM. These discrepancies result from the biases in the simulated cloud fraction and LWP in a complicated and combined way (Figs. 1 and 3).

Figure 8 shows a comparison of the seasonal mean LCF at the TOA simulated in the iRAM with CERES satellite observations. The geographical pattern of the LCF from the iRAM agrees with that from CERES measurements reasonable well over the eastern Pacific with high values in the ITCZ and the southwest region of the model domain. The model slightly underestimates the LCF by about 10 W m^{-2} in both regions. Similar to the bias of SCF in the seasonal cycle, the maximum LCF in the model is also delayed by one season in the ITCZ—from MAM in the observations to JJA in the simulation. Nevertheless, the geographical distribution in LCF is well captured by the model.

b. *Dynamical variables and physical processes*

Low clouds are controlled by dynamical and physical processes, including the large-scale subsidence in the eastern subtropical oceans, the seasonal variation of SST, the changes in lower-tropospheric stability, warm/cold advection in the planetary boundary layer, surface heat and moisture fluxes, vertical mixing in the subcloud layer, cloud-top entrainment, and so on. Therefore, examining the seasonal variations of these dynamical variables and the associated physical processes is the key to understanding the mechanisms responsible for the seasonal variation of MBL clouds.

1) SLP AND MIDTROPOSPHERIC VERTICAL VELOCITY

Figure 9 shows the seasonal mean sea level pressure (SLP) and vertical p velocity at 500 hPa simulated in the

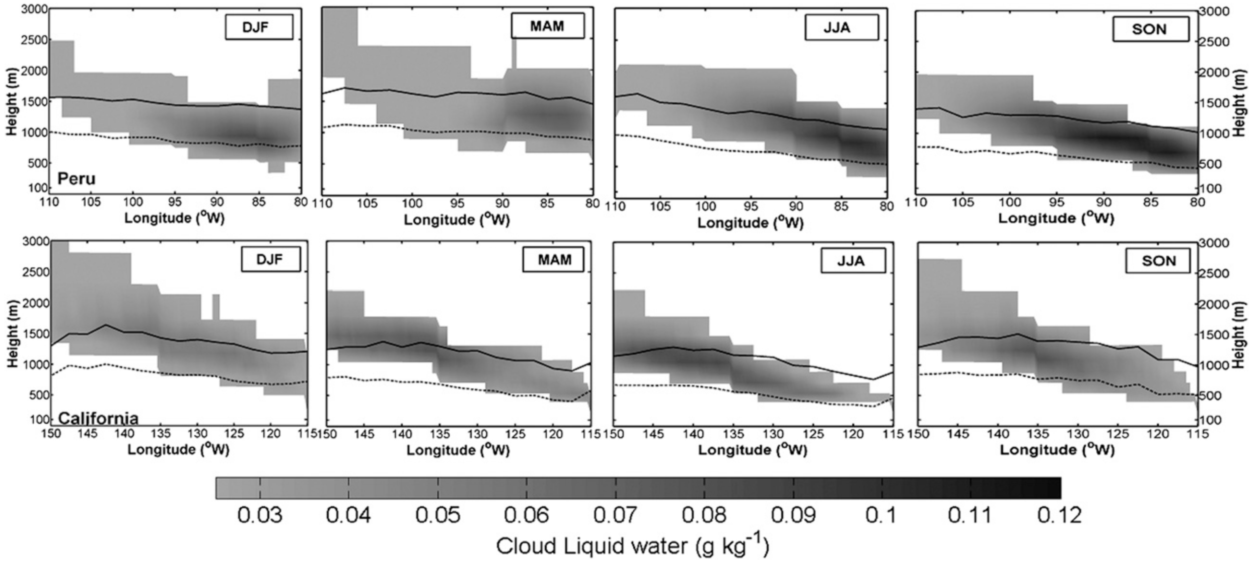

FIG. 6. Seasonal mean zonal-vertical cross sections of the modeled cloud liquid water content: (top) along 15°S off the Peru coast and (bottom) along 25°N off the California coast. Areas with liquid water content greater than 0.025 g kg^{-1} are shaded. Solid lines show the seasonal mean CALIPSO cloud-top heights. Dashed lines show the cloud-base heights.

iRAM, and those from the NCEP FNL analysis (and NCEP–NCAR reanalysis data prior to 2000; see section 2). High sea level pressure off the Peru and California coasts is associated with subtropical highs. We can see that the seasonal evolution of both the strength and position of the subtropical highs in both the southeast and northeast Pacific are well simulated in the iRAM. The low SLP associated with the ITCZ around 10°N is also captured by the model, although the minimum SLP is too low in the simulation, partly because of the coarser resolution of the reanalysis data and partly because of the overestimated precipitation in the ITCZ region in the model (not shown). Nevertheless, the seasonal variation of low pressure in the ITCZ in the simulation matches the FNL analysis/reanalysis quite well, consistent with the seasonal variation of convection in the ITCZ (not shown).

The subtropical high off the Peru coast over the southeast Pacific is the strongest in SON with an average SLP of 1023 hPa, concurrent with the maximum low-level cloudiness in this region and this season (Fig. 1). It is the

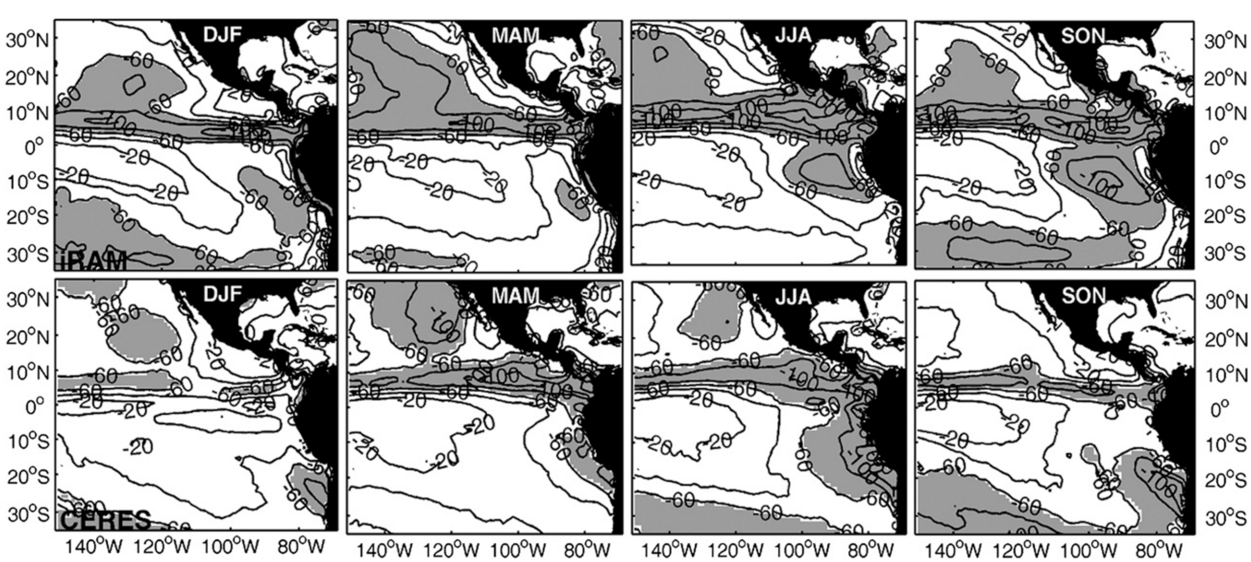

FIG. 7. Seasonal mean shortwave cloud radiative forcing at the TOA (W m^{-2}): (top) iRAM simulation and (bottom) CERES observation. Regions with values less than −60 W m^{-2} are shaded.

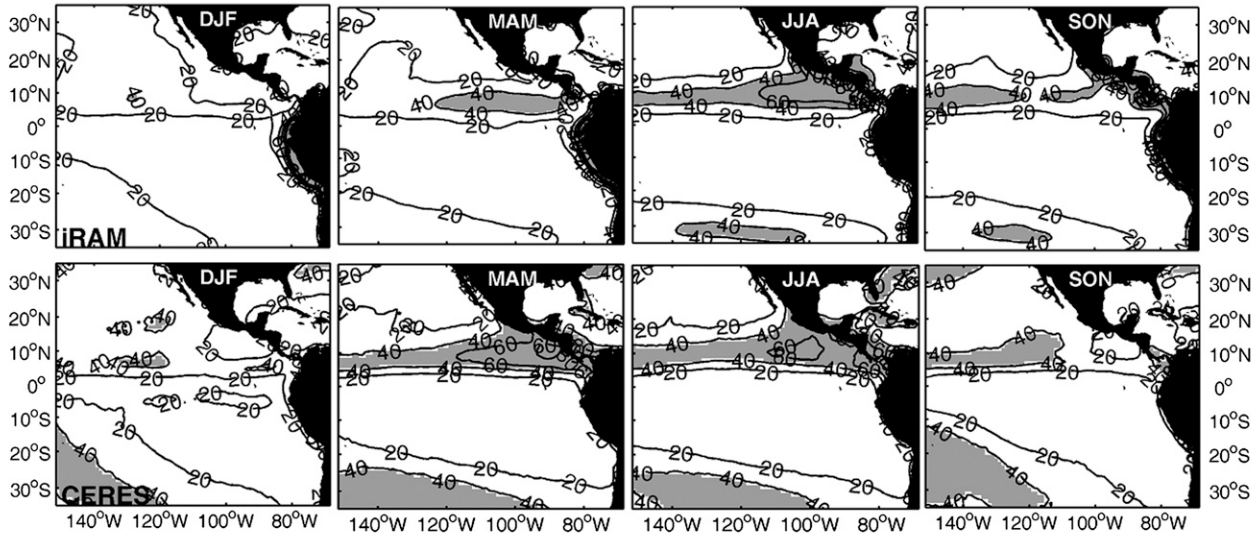

FIG. 8. Seasonal mean longwave cloud radiative forcing at the TOA (W m^{-2}): (top) iRAM simulation and (bottom) CERES observation. Regions with values larger than 40 W m^{-2} are shaded.

weakest in MAM, with an average SLP of 1020 hPa, coinciding with the minimum low-level cloudiness in the region. The subtropical high over the southeast Pacific reaches its southernmost position (33°S) in DJF and moves northeastward to its northernmost position in JJA (27°S).

The subtropical high off the California coast over the northeast Pacific is strongest in JJA with a SLP of 1024 hPa, which concurs with the maximum low-level cloudiness in the season. It is weakest in SON with a SLP of 1021 hPa, the season with the second smallest low-level cloudiness in the region (Fig. 1). Similar to the subtropical high over the southeast Pacific, the subtropical high over the northeast Pacific also reaches its southernmost position (30°N) in DJF. However, it moves northwestward, rather than northeastward, compared with its southeastern counterpart, and it reaches its northernmost position (36°N) in JJA.

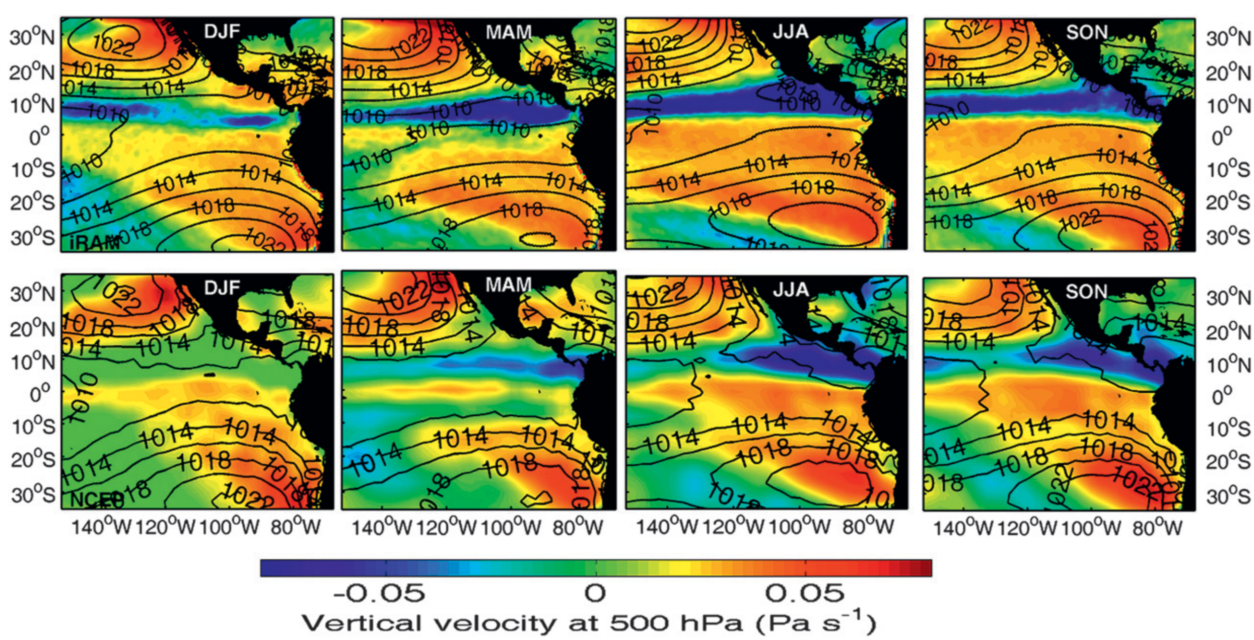

FIG. 9. Seasonal mean SLP (contours; hPa) and vertical p velocity at 500 hPa (shading; Pa s^{-1}): (top) iRAM simulation and (bottom) NCEP–NCAR analysis/reanalysis.

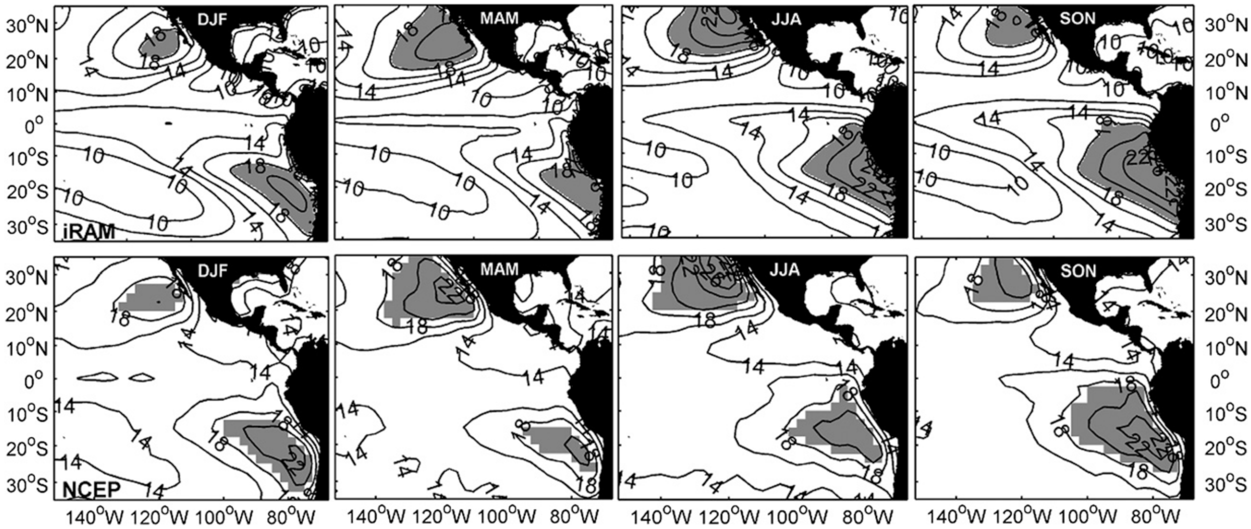

FIG. 10. Seasonal mean LTS (contours; K): (top) iRAM simulation and (bottom) NCEP–NCAR analysis/reanalysis. Regions with LTS greater than 18 K are shaded.

Vertical p-velocity at 500 hPa shows prevailing weak subsidence (about 0.03 Pa s^{-1}) in most of the subtropics and tropics south of the equator, with the strongest subsidence (exceeding 0.05 Pa s^{-1}) near the California and Peruvia coasts, namely, in the trade wind belts in the eastern regions of the subtropical highs. Seasonal mean ascending motion occurs in the ITCZ and in the region close to the southwestern border of the model domain. The latter is associated with the activity of synoptic-scale disturbances in the midlatitudes. The iRAM reproduces the subsidence associated with the subtropical highs reasonably well while overestimating the upward motion in the ITCZ region compared with the NCEP analysis/reanalysis. This is partly due to too strong convection and precipitation in the ITCZ in the model simulation.

2) LTS

LTS, which is defined as the difference in potential temperature between 700 and 1000 hPa ($\theta_{700\text{hPa}} - \theta_{1000\text{hPa}}$), has been found to be important to MBL clouds. Klein and Hartmann (1993) showed that stratus cloud amount is highly correlated with LTS, both seasonally and geographically. Figure 10 shows the LTS from the iRAM and the NCEP analysis/reanalysis. Regions with high LTS exceeding 18 K are found off the Peru and California coasts, coincident with the locations of the two stratocumulus decks. Off the Peru coast, LTS is strongest (22 K) in SON and weakest (20 K) in MAM, consistent with the seasons of maximum and minimum low-level cloudiness in this region. Similarly, LTS off the California coast is strongest (22 K) in JJA, with the maximum low-level cloudiness, and it is weakest (19 K) in DJF, with the minimum low-level cloudiness. Both the geographic pattern and the seasonal variation of the modeled LTS generally agree well with the NCEP analysis/reanalysis. Since the model's SST is prescribed based on observations, the general agreement in the simulated LTS with the analysis/reanalysis data indicates that the simulation of lower-tropospheric temperature is also in good agreement with the NCEP analysis/reanalysis.

To help understand the seasonal variation of LTS in the two stratocumulus regions, we show the seasonal mean vertical profiles of air temperature from the iRAM and those from the NCEP analysis/reanalysis at 15°S, 85°W and 25°N, 125°W in Fig. 11. Near the center of the Peruvian stratocumulus deck (15°S, 85°W), the amplitude of the seasonal variation of surface air temperature is larger than that of the air temperature above about 1000 m. The air temperature near the surface follows SST closely and varies between 15.6°C in SON and 22.0°C in MAM. This suggests that the seasonal variation of SST is more important than that of the free-tropospheric air temperature in determining the LTS in this region.

In contrast to the Peruvian low-level cloud region, the range of seasonal variation in the free-tropospheric air temperature is greater than that in surface air temperature in the California stratocumulus region (25°N, 125°W). The surface air temperature varies between 16.0°C in MAM and 19.4°C in SON, which is much smaller than the seasonal variation of the surface air temperature off the Peru coast. The air temperature at about 1500 m in the California region shows a much larger seasonal variation, with the minimum value of 9.8°C in DJF and the maximum value of 20.0°C in JJA, namely, over 10°C. This demonstrates that the seasonal variation of the free-tropospheric air temperature is more important than

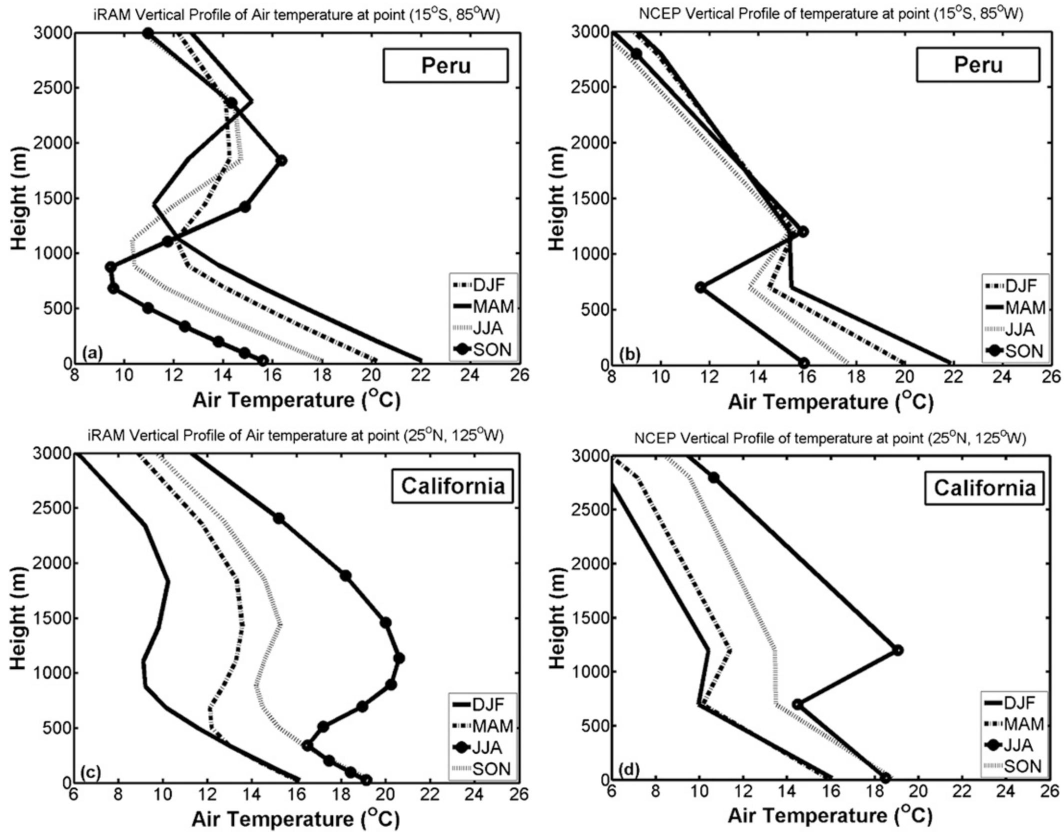

FIG. 11. Seasonal mean vertical profiles of air temperature at (top) 15°S, 85°W analysis/reanalysis and (bottom) 25°N, 125°W for (left) iRAM and (right) NCEP–NCAR analysis/reanalysis.

that of SST in determining LTS in the California stratocumulus region, which is consistent with the results in Klein and Hartmann (1993).

Note also from Fig. 11 that the lower the temperature inversion layer, the stronger the inversion, which is consistent with higher low-level cloud amount (Fig. 1) and a larger LWP (Fig. 3) in both stratocumulus regions. Furthermore, although the NCEP analysis/reanalysis gives reasonable LTS, as shown in Fig. 10, it cannot resolve the seasonal variation in inversion height well, partly because of its coarse vertical resolution.

3) OCEAN SURFACE WINDS AND NEAR-SURFACE TEMPERATURE ADVECTION

Previous studies have already shown that cold advection near the surface is important for determining surface fluxes and thus the characteristics of MBL clouds over the subtropical oceans (e.g., Klein et al. 1995; Klein 1997). The cold advection increases surface latent heat and sensible heat fluxes, causing a destabilization of the MBL, stronger overturning and moisture transport into the cloud layer, and thicker clouds (Xu et al. 2005). Since the horizontal gradient of near-surface air temperature is close to that of SST in the studied region, this effect can be studied using the so-called SST advection, which is defined as the advection of SST by 10-m winds ($\mathbf{V}_{10\mathrm{m}}$), namely, ($-\mathbf{V}_{10\mathrm{m}} \cdot \nabla \mathrm{SST}$). SST advection is found to be strongly correlated with the low-level stratiform cloud amount over the subtropical oceans on synoptic-to-seasonal and subseasonal time scales (e.g., Klein et al. 1995; Klein 1997; Norris and Iacobellis 2005; Xu et al. 2005). Since SST is prescribed in the simulation, SST advection is determined predominantly by the surface winds. Therefore, we first compare the surface winds from the model simulation with those from QuikSCAT measurements over the ocean. Figure 12 shows the seasonal mean surface wind speeds and wind vectors for the period from July 1999 through December 2008, the period with QuikSCAT surface wind data available.

Surface winds are driven by pressure gradients associated with the subtropical highs in both hemispheres in the studied region and are dominated by trade winds (southeasterly in the Southern Hemisphere and northeasterly in the Northern Hemisphere) in the eastern subtropical oceans. The iRAM generally simulates the surface winds comparable with the QuikSCAT observations,

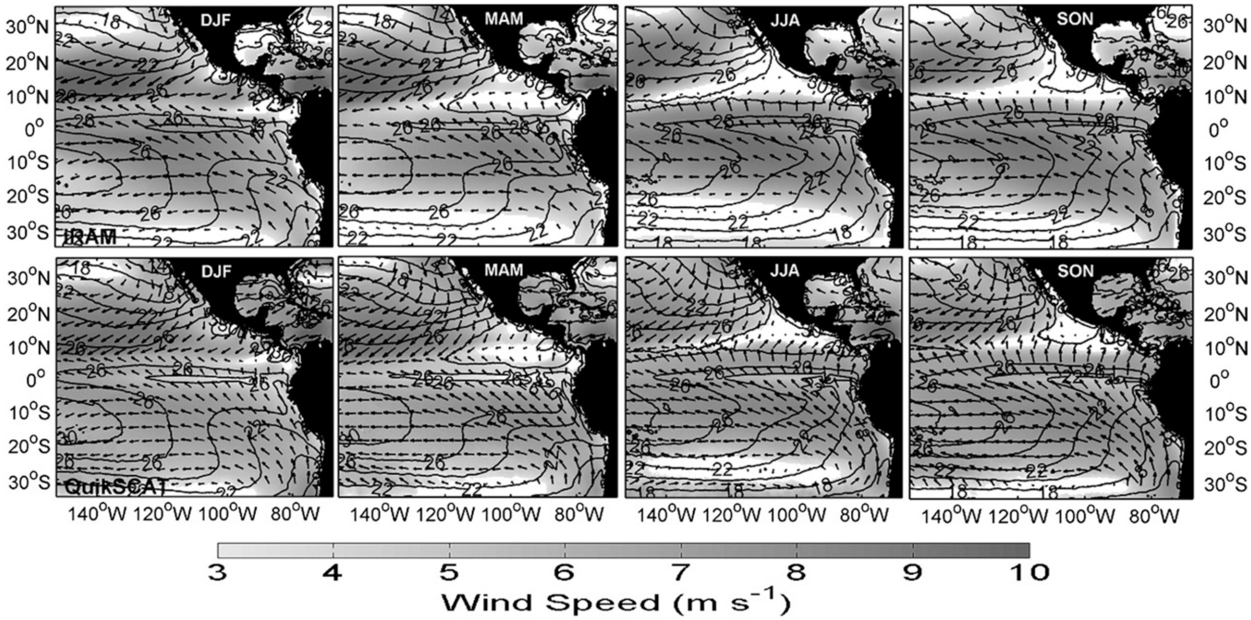

FIG. 12. Seasonal mean surface wind vectors and wind speed (shading; m s^{-1}): (top) iRAM simulation and (bottom) QuikSCAT observations. Contours show seasonal mean SST (°C).

except for an overestimation of trade winds and winds in the tropics by about 1.0 m s^{-1} and a small underestimation of the southerlies along the Peru coast, particularly south of 20°S. The latter might be partly due to the coarse horizontal model resolution, which is not high enough to resolve the high and steep Andes and the land–sea contrast well.

SST off the Peru coast peaks at about 23.7°C in MAM (Fig. 12), coinciding with the minimum low-level cloudiness, and reaches its minimum of about 19.6°C in SON during the season with the maximum low-level cloudiness in the region (Fig. 1). However, the relationship between the seasonal variations of SST and low-level cloudiness is different in the California region, where SST varies from about 20.5°C in MAM to 23.1°C in SON. Low-level cloud amounts are smaller in DJF, when SSTs are colder, than in JJA, when with warmer SSTs are warmer. This is already reflected in the weak dependence of LTS on SST in this region and in the close correlation between variations of LTS and lower-tropospheric air temperature, as discussed above (Fig. 11).

The large angles between surface wind vectors and SST gradient near the coastal regions off Peru and California and in the tropical and subtropical regions in Fig. 12 imply strong cold SST advection in most regions with trade winds, except for a narrow region north of the equator associated with the equatorial cold tongue in the eastern Pacific. The calculated SST advections from iRAM and QuikSCAT winds agree fairly well (Fig. 13). Cold SST advections with values from $-1°$ to $-2.0°$C day^{-1} prevail over most of the model domain in all seasons. Such cold advections are more pronounced off the Peru coast than off the California coast and show a significant seasonal variation.

4) COLUMN WATER VAPOR AND LATENT HEAT FLUX

Since water vapor in the atmosphere usually decreases exponentially with height above the boundary layer, column water vapor primarily reflects the depth of the boundary layer. This is particularly the case in the subtropical eastern oceans (e.g., Wang et al. 2004b). On the other hand, surface latent heat flux has been shown to be critical to both the maintenance of MBL cloud and the degree of decoupling of the MBL and thus the transition from stratocumulus to trade cumulus clouds offshore in the eastern subtropical oceans (Wyant et al. 1997; Bretherton and Wyant 1997). Therefore, realistic simulations of both variables are crucial to the skillful simulation of seasonal variation of MBL clouds by an atmospheric model.

The simulated seasonal mean column-integrated water vapor in iRAM is in good agreement with SSM/I measurements (Fig. 14). The seasonal variation of column water vapor is generally consistent with that of SST (Fig. 12) and the cloud-base height (Fig. 4) in both observations and the simulation. Off the Peru coast, the column water vapor peaks at around 2.7 cm in MAM, the season of the warmest SST, the minimum low-level cloudiness, and the highest cloud-base height. It reaches the minimum

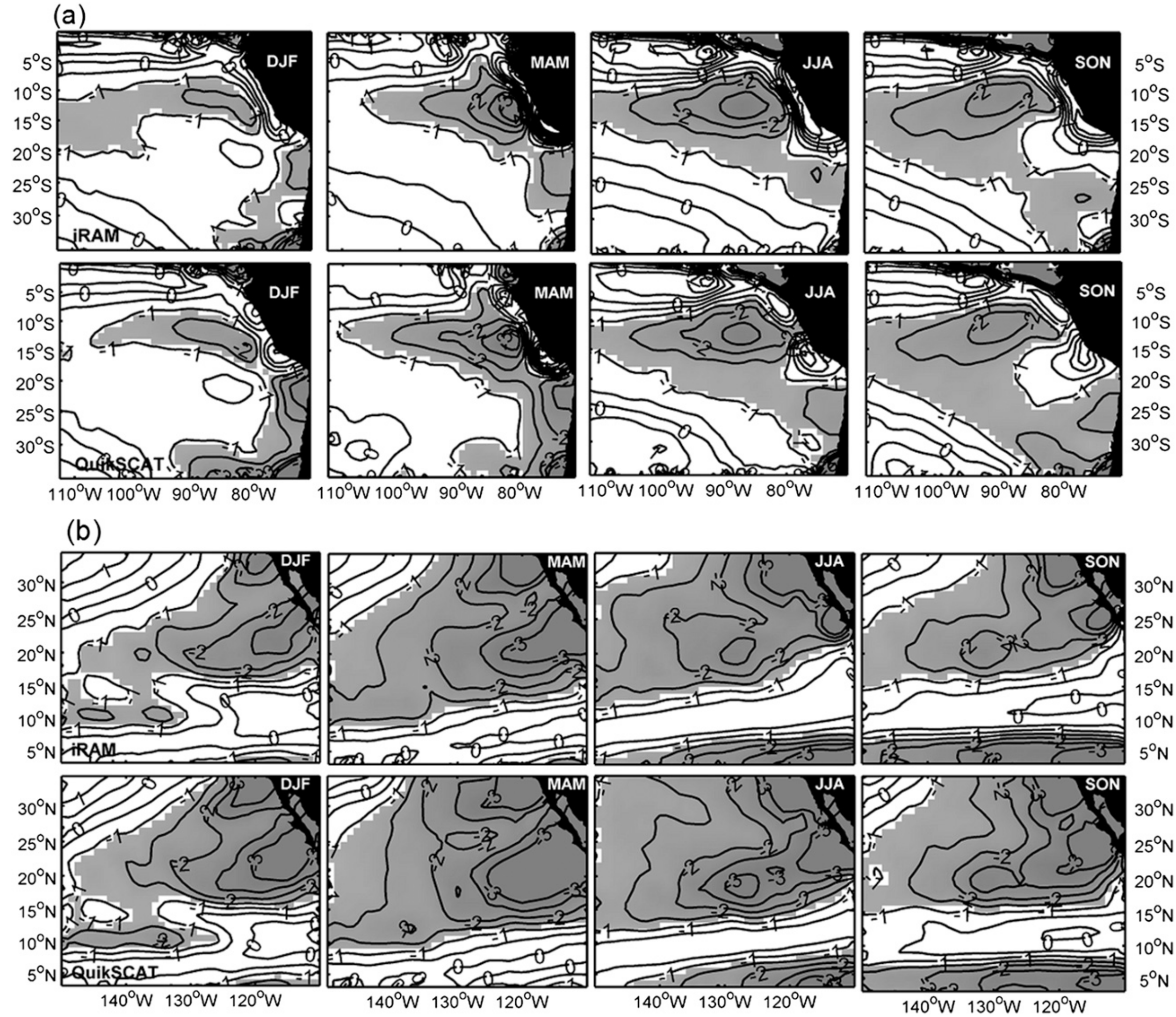

FIG. 13. Seasonal mean SST advection (K day^{-1}) calculated using the simulated surface winds in [top rows in (a),(b)] iRAM and [bottom rows in (a),(b)] observed surface winds from the QuikSCAT satellite off the (a) Peru and (b) California coasts.

value of about 1.8 cm in SON, the season of the coldest SST, the maximum low-level cloudiness, and the lowest cloud-base height. Off the California coast, the column water vapor reaches the maximum value of around 2.2 cm in JJA and the minimum value of 1.8 cm in DJF. In sharp contrast to the region off the Peru coast, the low-level cloudiness is highest in JJA with the largest column water vapor, while it is lowest in DJF with the minimum column water vapor. This implies that the free-tropospheric water vapor contributes significantly to the column water vapor in the region off the California coast because the free-atmospheric air temperature shows a greater increase from DJF to JJA than SST in this region (Fig. 11).

A comparison of the simulated seasonal mean surface latent heat flux by iRAM and from the OAFlux dataset is also shown in Fig. 14. Off the Peru coast, the surface latent heat flux from the OAFlux dataset peaks at around 116.5 W m^{-2} in MAM, the season with the minimum low-level cloudiness, and reaches its minimum value of 93.0 W m^{-2} in SON, the season with the maximum low-level cloudiness. Off the California coast, the maximum surface latent heat flux in the OAFlux dataset (124.4 W m^{-2}) is found in DJF, the season with the minimum low-level cloudiness, and reaches its minimum of 89.3 W m^{-2} in JJA—again, the season with the maximum low-level cloudiness. The relationship between the seasonal variation of low-level cloud amount and that of the surface latent heat flux is similar in both the Peruvian and the California MBL cloud regions, namely, the season with the maximum (minimum) low-level cloudiness

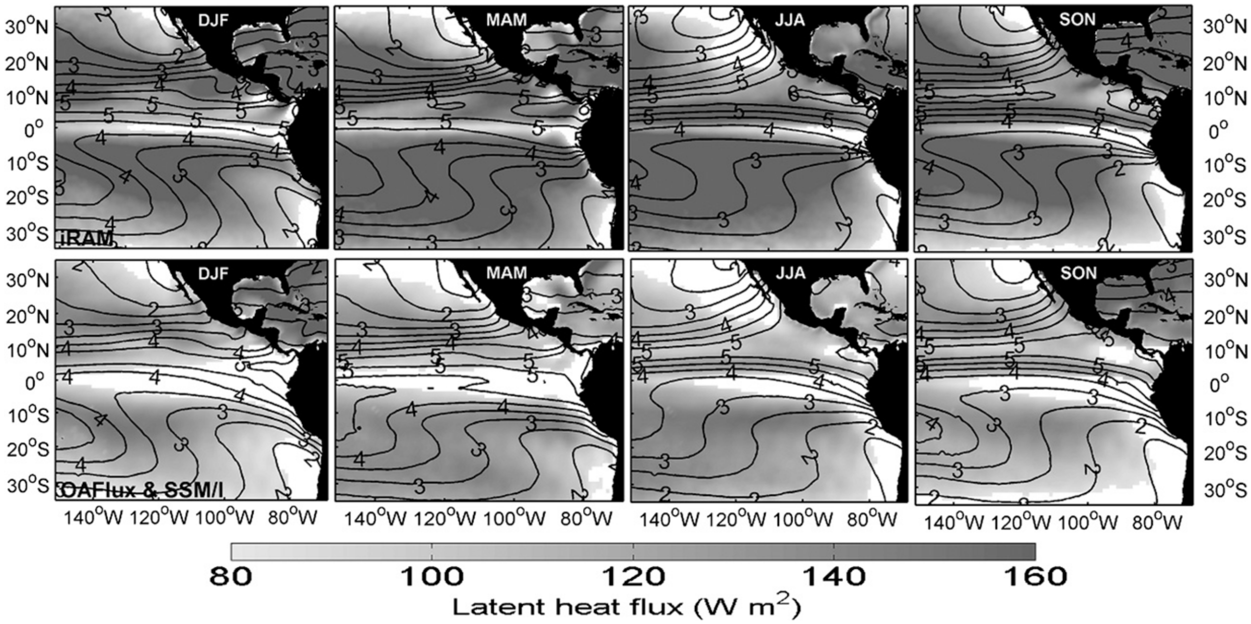

FIG. 14. Seasonal mean surface latent heat flux (shading; W m^{-2}) and column water vapor (contours; cm): (top) iRAM simulation and (bottom) OAflux data for latent heat flux and SSM/I satellite observations for column water vapor.

corresponds to the season with the lowest (highest) surface latent heat flux. This is primarily because the well-mixedcloud-topped MBL generally has a moister subcloud layer and colder SST, both suppressing the surface latent heat flux. The large surface latent heat flux indicates a higher SST, a drier subcloud layer, and a boundary layer that is more often decoupled (Wyant et al. 1997; Bretherton and Wyant 1997; see further discussion in section 4). The iRAM overestimates the surface latent heat flux over the Peruvian and California stratocumulus regions by about 30–50 W m^{-2} compared with the OAFlux dataset. This could be caused by the bias in the simulated too strong surface winds and air–sea humidity differences in the model. Nevertheless, the model reproduces the seasonal variation and spatial distribution of the surface latent heat flux reasonably well.

5) MBL MIXING

To assess the degree of MBL mixing, we analyzed the difference in total water mixing ratios between the surface $(q_t)_{\text{surface}}$ and the cloud-base height $(q_t)_{\text{CB}}$ following Wyant et al. (1997):

$$\Delta q = (q_t)_{\text{surface}} - (q_t)_{\text{CB}}. \tag{1}$$

A small value of Δq indicates a high degree of mixing in the MBL, whereas a large value indicates a low degree of mixing as well as the possibility of internal boundary layer stratification and vertical decoupling. Cloud and subcloud layers are generally more likely to be decoupled in a not well-mixed MBL than in a well-mixed MBL. Note that in addition to turbulence mixing, many other processes may affect moisture profile (thus Δq), including midlatitude synoptic disturbances in winter seasons. Nevertheless, regardless of what processes cause the changes in Δq, it can be considered an indication of MBL decoupling and cloud regime transition, as demonstrated by Wyant et al. (1997) and Bretherton and Wyant (1997).

We calculated Δq from the daily mean values of model output and then averaged it over each season (Fig. 15). Small Δq values of less than 0.8 g kg^{-1} appear near the coasts, indicating little decoupling of the MBL, particularly in SON in the southeast Pacific and in JJA in the northeast Pacific, where we find the shallowest MBL and the lowest cloud-base and cloud-top heights (Figs. 4 and 6). Downwind to the west, Δq increases and reaches values exceeding 1.4 g kg^{-1}, indicating a transition from a coupled to a decoupled MBL, consistent with previous studies based on observations (e.g., Albrecht et al. 1995a; Betts et al. 1995). Deepening of the boundary layer downwind of the subtropical stratocumulus regions usually coincides with increased decoupling of the MBL. This agrees with the ''deepening–decoupling'' hypothesis of Bretherton and Wyant (1997), in which the stratocumulus-to-trade-cumulus transition is directly linked to the deepening and decoupling boundary layer over warmer oceans. The general distribution of Δq in SON is similar to the results for the decoupling parameters α_θ and α_q estimated by Wood and Bretherton (2004) for September–October 2000.

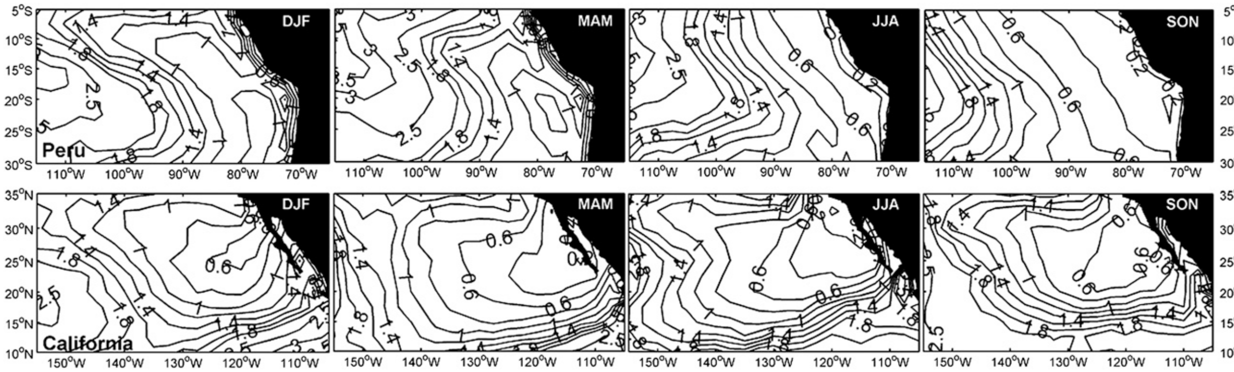

FIG. 15. Seasonal mean of difference in total water content between the surface and cloud base (Δq; g kg^{-1}) from iRAM: off the (top) Peru and (bottom) California coasts.

The model Δq shows a distinct seasonal variation in both the Peruvian and California MBL cloud regions. Off the Peru coast, the mean value of Δq peaks in MAM (1.5 g kg^{-1}) and reaches its minimum value of 0.5 g kg^{-1} in SON. Off the California coast, the mean value of Δq is largest in DJF (0.9 g kg^{-1}) and smallest in JJA (0.6 g kg^{-1}). The season of maximum low-level cloudiness corresponds to the season of the smallest Δq, suggesting that a well-mixed MBL tends to maintain extensive low cloud decks. The low-level cloud amount is reduced in both regions in seasons with larger Δq and thus a higher degree of MBL decoupling.

6) CLOUD-TOP ENTRAINMENT RATE

Entrainment is the mixing of filaments or blobs of overlying nonturbulent air into the MBL by turbulent eddies occurring in a thin entrainment zone near the cloud top. The entrainment rate w_e at which air is mixed into the MBL is a crucial parameter for the evolution of MBL clouds because it determines the magnitude of the warming and drying of the MBL by the incorporation of free-tropospheric air (Lilly 1968; Deardorff 1976). Entrainment of warm and dry free-tropospheric air can change the thermodynamic structure of the boundary layer and lead to cloud-top evaporation that can significantly modify the cloud field (e.g., Moeng 2000; Lock 2009). The mean entrainment rate at the top of the MBL can be estimated by

$$\frac{\partial z_i}{\partial t} + u(z_i) \cdot \nabla z_i = w_e - w_s(z_i), \qquad (2)$$

where z_i is the boundary layer depth, $u(z_i)$ is the horizontal wind velocity, w_e is the entrainment rate, and $w_s(z_i)$ is the subsidence rate at the top of the boundary layer. Averaging Eq. (2) over a sufficiently long period of time, such as a whole season, and considering that $\partial \overline{z_i}/\partial t = 0$ and $\overline{u'(z_i) \cdot \nabla z_i'} \ll \overline{u(z_i)} \cdot \nabla \overline{z_i}$, we obtain

$$\overline{w_e} \approx \overline{u(z_i)} \cdot \nabla \overline{z_i} + \overline{w_s(z_i)}. \qquad (3)$$

The seasonal mean w_e at the cloud top estimated from the model results according to Eq. (3) is presented in Fig. 16. Analysis of the three individual terms in Eq. (3) shows that the entrainment rate is largely determined by the subsidence rate, whereas the advection term $[\overline{u(z_i)} \cdot \nabla \overline{z_i}]$ is generally small. The average w_e calculated

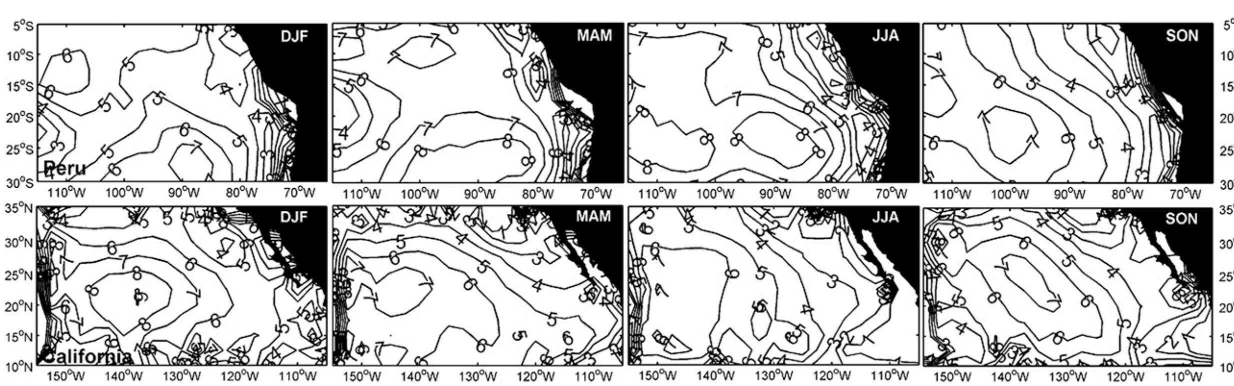

FIG. 16. Seasonal mean entrainment rate (mm s^{-1}) at cloud top simulated in iRAM: off the (top) Peru and (bottom) California coasts.

from the model results in the two stratocumulus regions range between 2 and 9 mm s^{-1}. The mean w_e shows a distinct seasonal variation in both the Peruvian and California MBL cloud regions. Off the Peru coast, the mean value of w_e peaks in MAM at about 6.7 mm s^{-1} and reaches its minimum value of 4.3 mm s^{-1} in SON. Off the California coast, the mean w_e reaches its maximum value of 7.1 mm s^{-1} in DJF and its minimum value of 4.6 mm s^{-1} in JJA. The season of the maximum low-level cloudiness coincides with the season of the minimum w_e, suggesting that weaker entrainment favors more persistent low clouds. In seasons with large entrainment, low-level cloud amounts are reduced in both the Peruvian and California stratocumulus regions.

We compared the mean w_e estimated from the NCEP reanalysis and satellite observations by Wood and Bretherton (2004) for the 2-month period of September–October 2000 with the results from the iRAM for SON 2000 and found that the iRAM estimated entrainment rates in SON off the Peru coast agree well with the results of Wood and Bretherton (2004), showing an increase of w_e from the coast toward the open ocean. The results from Wood and Bretherton (2004) show the maximum w_e in the California region between 120° and 130°W, whereas the maximum w_e is located 10° farther to the west in the iRAM, which is due to a westward shift of the modeled stratocumulus deck in the iRAM in this region. Averaged over the same region, the model w_e is about 0.5 mm s^{-1} larger in the California region and 1.3 mm s^{-1} larger in the Peruvian region than the corresponding results of Wood and Bretherton (2004). Since the model used to produce the reanalysis generally underestimates the stratocumulus cloud amount, the cloud-top entrainment estimated from the reanalysis in Wood and Bretherton (2004) might be underestimated. Therefore, results from the iRAM could be considered to give a good estimation of entrainment rate.

4. Discussion

In this section, we discuss and highlight the physical mechanisms responsible for the seasonal variations of MBL clouds in the Peruvian and California regions by contrasting various parameters/variables between the seasons with the maximum and minimum low-level cloudiness. In the Peruvian region, SON (austral spring) and MAM (austral fall) are the seasons with the maximum and minimum low-level cloudiness, respectively. Table 1 summarizes the relevant physical parameters from the model averaged over 25°–5°S, 100°–75°W for SON and MAM. In SON, the mean low-level cloudiness is about 24% higher, the SST is 4.1°C colder, and the air temperature at 700 hPa is 1.2°C colder than in MAM.

TABLE 1. Simulated 12-yr mean (1997–2008) of physical parameters over the Peruvian stratocumulus region (25°–5°S, 100°–75°W) for austral spring and autumn.

Parameter	SON (austral spring)	MAM (austral autumn)
Low cloud amount (%)	64.6	40.6
SST (°C)	19.6	23.7
Air temperature at 700 hPa (°C)	8.2	9.4
Latent heat flux (W m^{-2})	125.2	165.4
Cloud-base height (m)	548.8	1019.8
Cloud-top height (m)	1257.0	1835.4
Low-cloud thickness (m)	708.2	815.7
Δq (g kg^{-1})	0.5	1.4
w_e (mm s^{-1})	3.9	6.3

The mean latent heat flux in SON is 40 W m^{-2} smaller than in MAM, the mean cloud-base height is 500 m lower, and the mean cloud-top height is 620 m lower than in MAM. The mean cloud thickness is about 120 m thinner in SON than in MAM. The mean Δq is about 0.9 g kg^{-1} smaller in SON than in MAM, and the mean cloud-top entrainment rate is about 2.4 mm s^{-1} smaller in SON than in MAM, indicating a higher degree of mixing in the subcloud layer and a less likely occurrence of decoupling of the MBL in SON than in MAM.

In the California coastal region, JJA (boreal summer) and DJF (boreal winter) are the seasons with the maximum and minimum low-level cloudiness, respectively. Table 2 summarizes the relevant physical parameters from the model averaged over 15°–30°N, 140°–120°W for JJA and DJF. The low-level cloudiness is higher in JJA than in DJF (58% versus 45%), with the mean SST being 1.5°C warmer and the mean air temperature at 700 hPa being 3.6°C warmer in JJA than in DJF. The amplitude of seasonal variation of lower-tropospheric air temperature is larger than that of SST, in contrast to that in the Peru coastal region, where the seasonal variation of SST is larger. Despite warmer SSTs, the mean latent heat flux is about 35 W m^{-2} smaller in JJA than in DJF. The mean cloud-base height is 450 m and the mean cloud-top height is 670 m lower in JJA than in DJF. The mean cloud thickness is thus 220 m thinner in JJA than in DJF. The mean Δq is 0.4 g kg^{-1} smaller in JJA than in DJF, and the mean cloud-top entrainment rate is 2.3 mm s^{-1} smaller in JJA than in DJF, indicating a higher degree of subcloud-layer mixing and less decoupling of the MBL in JJA than in DJF.

Because air masses are advected from the subtropical stratocumulus region toward warmer water downwind, MBL clouds are usually subject to a cloud regime transition from stratocumulus to trade cumulus. The transition is accompanied by a deepening and decoupling of the

TABLE 2. Twelve-year means (1997–2008) of simulated physical parameters in the California stratocumulus region (15°–30°N, 140°–120°W) for boreal winter and summer.

Parameter	JJA (boreal summer)	DJF (boreal winter)
Low cloud amount (%)	58.2	45.1
SST (°C)	22.4	20.9
Air temperature at 700 hPa (°C)	9.3	5.7
Latent heat flux (W m^{-2})	119.3	154.4
Cloud-base height (m)	502.7	956.9
Cloud-top height (m)	1136.0	1805.2
Low-cloud thickness (m)	633.3	848.3
Δq (g kg^{-1})	0.7	1.1
w_e (mm s^{-1})	4.9	7.2

MBL, the development of trade cumuli below the stratocumulus, and the gradual dissipation of the overlying stratocumulus (Albrecht et al. 1995b). This well-known transition has been studied using in situ observations (e.g., Betts and Boers 1990; Bretherton and Pincus 1995; de Roode and Duynkerke 1997), satellite observations, and operational weather analysis (e.g., Pincus et al. 1997; Sandu et al. 2010). Bretherton and Wyant (1997) described a deepening–decoupling mechanism to explain the observed stratocumulus-to-cumulus transition. As the SST rises relative to the air above the inversion when the air is being advected over warmer water, the boundary layer deepens and the surface latent heat flux increases, leading to the decoupling of the MBL (see also Wyant et al. 1997). Once the cloud and subcloud layers are decoupled, cloud cover remains high but the cloud regime changes from a single stratocumulus layer to sporadic cumulus beneath stratocumulus. As the SST rises further and the boundary layer deepens, cumulus convection becomes vigorous and entrains significant dry air from above the inversion into the MBL. The stratocumulus then gradually evaporates and thins because of increased entrainment at the cloud top and reduced moisture supply from the surface. This will finally result in the breakup and dissipation of the stratocumulus. The MBL becomes a trade wind cumulus boundary layer after the complete dissipation of the overlying stratocumulus.

Based on multisatellite data analysis, Lin et al. (2009) recently proposed that the seasonal variation of low-level cloud properties off the California coast resembles the downstream stratocumulus-to-cumulus transition driven by the deepening–decoupling mechanism of Bretherton and Wyant (1997). Our analysis of the relevant physical parameters off the Peruvian and California coasts in the model suggests that the characteristics of the seasonal variation of low-level clouds in both regions are similar to that of the spatial variation associated with the stratocumulus-to-cumulus transition as well. These include the interplay among low-level cloud amount, surface latent heat flux, cloud-base and cloud-top heights or cloud thickness, cloud-top entrainment, and decoupling, as we have summarized in Tables 1 and 2 and discussed above.

In the season with the minimum low-level cloudiness, the latent heat flux is the largest and the cloud-base and cloud-top heights are the highest among four seasons, implying a high degree of decoupling. This is consistent with a deep boundary layer with the largest difference of total water mixing ratios between the surface and the cloud base and the maximum entrainment rate at the cloud top in the season. In contrast, in the season with the maximum low-level cloudiness, the latent heat flux is the smallest and the cloud-base and cloud-top heights are the lowest, implying a coupled, shallow, and well-mixed MBL with small entrainment rates at the cloud top.

The seasonal variation of MBL clouds in both the Peruvian and California regions is thus very similar to the deepening–decoupling previously used to describe the spatial cloud transition from the stratocumulus to cumulus (Bretherton and Wyant 1997; Wyant et al. 1997). However, although the same mechanism applies to both regions, the processes leading to the decoupling are different in the two regions. In the former region, the seasonal variation of SST dominates, while in the latter region, the seasonal variation of lower-tropospheric air temperature dominates to determine the LTS and thus the evolution of the MBL and the low clouds. This is consistent with Lin et al. (2009), who suggested that the seasonal warming in SST is small relative to the free-tropospheric air temperature in the California region. In contrast, the warming in SST in the Peruvian region does not need to be taken as relative to the free-tropospheric air temperature because of the larger amplitude of the seasonal SST variation than that of the free-tropospheric air temperature. The free-tropospheric air temperature shows more significant seasonal variations than the SST in the California region, because the California stratocumulus deck is at a higher latitude and hence undergoes a larger seasonal cycle in the free-tropospheric air temperature. The weaker seasonal cycle in SST off the California coast is associated with the northward displacement of the ITCZ. The amplitude of the seasonal SST cycle has been found to be the minimum along the climatological ITCZ and increases poleward from the ITCZ (Xie 2004).

5. Summary

The seasonal variation of MBL clouds over the eastern Pacific simulated in the iRAM was examined in this study. Comparisons with observations show that the model is capable of simulating not only the overall seasonal variation but also the spatial distribution, cloud regime transition, and vertical structure of MBL clouds over the eastern Pacific. In particular, the model reproduced major features of the seasonal variation in both stratocumulus decks off the Peruvian and California coasts, although the position of the modeled stratocumulus deck is shifted by about 8° to the northwest for the former region and by 9° to the west for the latter region compared with observations. Although the modeled MBL cloud layer is generally too high over the open ocean compared with available satellite observations, the model simulates well the westward deepening and decoupling of the MBL, the westward rise of the low cloud decks, and the cloud regime transition from stratocumulus near the coast to trade cumulus clouds farther to the west in both the southeast and northeast Pacific.

The realistic simulation of the seasonal variation of MBL clouds is attributed to the model's skill in reproducing many dynamical and physical processes well, including large-scale subsidence, LTS, and SST advection. The most important factor for our model to perform well is its use of the modified Tiedtke parameterization to represent shallow convection (McCaa and Bretherton 2004; Wang et al. 2004a,b). Although the model overestimates surface wind speeds by about 1 m s^{-1} or about 10%–15% and the surface latent heat flux by about 15%–20%, the model simulated well the seasonal variations in the degree of vertical decoupling of the MBL and the cloud-top entrainment rate. Both observations and model results show that in seasons with small low-level cloudiness, the latent heat flux is large and the cloud layer is high, with small subcloud mixing and strong entrainment at the cloud top, characterized by a relatively high degree of decoupling of the MBL, and vice versa.

This ''deepening–decoupling'' of the MBL is found to explain well the seasonal variation of MBL clouds in both the Peruvian and California regions, similar to the transition from the stratocumulus to cumulus westward off the Peru and California coasts. However, the processes leading to the decoupling are different in the two regions. Off the Peru coast, the seasonal variation of SST dominates that of the LTS and thus the evolution of the MBL and low clouds, while off the California coast, the seasonal variation of lower-tropospheric air temperature is more important than that of the SST. Results from this study are encouraging and demonstrate that the iRAM is a good tool to improve our understanding of low-cloud variability in the eastern Pacific. Indeed, we also found a close relationship among the interannual variation of low-level cloud amount, surface latent heat flux, cloud-top and cloud-base heights, cloud-top entrainment, and decoupling in both stratocumulus decks in our simulation. A detailed analysis on interannual variations focusing on the response of MBL clouds to the ENSO cycle is under way, and the results will be reported separately.

Acknowledgments. The authors are grateful to the two anonymous reviewers, whose constructive comments helped improve the presentation of the manuscript. This research was supported by NOAA/CPPA Grant NA07OAR4310257 and DOE Regional and Global Climate Modeling (RCGM) Program Grant ER64840. Additional support was provided by the Japan Agency for Marine-Earth Science and Technology (JAMSTEC), NASA Grant NNX07AG53G, and NOAA Grant NA09OAR4320075, which sponsor research at the International Pacific Research Center.

REFERENCES

Albrecht, B. A., C. S. Bretherton, D. Johnson, W. H. Schubert, and A. S. Frisch, 1995a: The Atlantic Stratocumulus Transition Experiment—ASTEX. *Bull. Amer. Meteor. Soc.,* **76,** 889–903.

——, M. P. Jensen, and W. J. Syrett, 1995b: Marine boundary layer structure and fractional cloudiness. *J. Geophys. Res.,* **100,** 14 209–14 222.

Bender, F. A.-M., H. Rodhe, R. J. Charlson, A. M. L. Ekman, and N. Loeb, 2006: 22 views of the global albedo—Comparison between 20 GCMs and two satellites. *Tellus,* **58A,** 320–330, doi:10.1111/j.1600-0870.2006.00181.x.

Betts, A. K., and R. Boers, 1990: A cloudiness transition in a marine boundary layer. *J. Atmos. Sci.,* **47,** 1480–1497.

——, C. S. Bretherton, and E. Klinker, 1995: Relation between mean boundary-layer structure and cloudiness at the R/V *Valdivia* during ASTEX. *J. Atmos. Sci.,* **52,** 2752–2762.

Bony, S., and J. L. Dufresne, 2005: Marine boundary layer clouds at the heart of tropical cloud feedback uncertainties in climate models. *Geophys. Res. Lett.,* **32,** L20806, doi:10.1029/2005GL023851.

Bretherton, C. S., and R. Pincus, 1995: Cloudiness and marine boundary layer dynamics in the ASTEX Langrangian experiments. Part I: Synoptic setting and vertical structure. *J. Atmos. Sci.,* **52,** 2707–2723.

——, and M. C. Wyant, 1997: Moisture transport, lower-tropospheric stability, and decoupling of cloud-topped boundary layers. *J. Atmos. Sci.,* **54,** 148–167.

——, J. R. McCaa, and H. Grenier, 2004a: A new parameterization for shallow cumulus convection and its application to marine subtropical cloud-topped boundary layers. Part I: Description and 1D results. *Mon. Wea. Rev.,* **132,** 864–882.

——, and Coauthors, 2004b: The EPIC 2001 stratocumulus study. *Bull. Amer. Meteor. Soc.,* **85,** 967–977.

Clement, A. C., R. Burgmann, and J. R. Norris, 2009: Observational and model evidence for positive low-level cloud feedback. *Science,* **325,** 460–464.

de Roode, S. R., and P. G. Duynkerke, 1997: Observed Langrangian transition of stratocumulus into cumulus during ASTEX: Mean state and turbulence structure. *J. Atmos. Sci.,* **54,** 2157–2173.

de Szoeke, S. P., and S.-P. Xie, 2008: The tropical eastern Pacific seasonal cycle: Assessment of errors and mechanisms in IPCC

AR4 coupled ocean–atmosphere general circulation models. *J. Climate,* **21,** 2573–2590.

——, Y. Wang, S.-P. Xie, and T. Miyama, 2006: Effect of shallow cumulus convection on the eastern Pacific climate in a coupled model. *Geophys. Res. Lett.,* **33,** L17713, doi:10.1029/2006GL026715.

Deardorff, J. W., 1976: On the entrainment rate of a stratocumulus topped mixed layer. *Quart. J. Roy. Meteor. Soc.,* **102,** 563–582.

Edwards, J. M., and A. Slingo, 1996: Studies with a flexible new radiation code. I: Choosing a configuration for a large-scale model. *Quart. J. Roy. Meteor. Soc.,* **122,** 689–719.

Gregory, D., J. J. Morcrette, C. Jakob, A. C. M. Beljaars, and T. Stockdale, 2000: Revision of convection, radiation and cloud schemes in the ECMWF Integrated Forecasting System. *Quart. J. Roy. Meteor. Soc.,* **126,** 1685–1710.

Hartmann, D. L., M. E. Ockert-Bell, and M. L. Michelsen, 1992: The effect of cloud type on earth's energy balance: Global analysis. *J. Climate,* **5,** 1281–1304.

Kalnay, E., and Coauthors, 1996: The NCEP/NCAR 40-Year Reanalysis Project. *Bull. Amer. Meteor. Soc.,* **77,** 437–471.

Klein, S. A., 1997: Synoptic variability of low-cloud properties and meteorological parameters in the subtropical trade wind boundary layer. *J. Climate,* **10,** 2018–2039.

——, and D. L. Hartmann, 1993: The seasonal cycle of low stratiform clouds. *J. Climate,* **6,** 1587–1606.

——, ——, and J. R. Norris, 1995: On the relationships among low-cloud structure, seas surface temperature, and atmospheric circulation in the summertime northeast Pacific. *J. Climate,* **8,** 1140–1155.

Lauer, A., Y. Wang, V. T. J. Phillips, C. S. McNaughton, R. Bennartz, and A. D. Clarke, 2009: Simulating marine boundary layer clouds over the eastern Pacific in a regional climate model with double-moment cloud microphysics. *J. Geophys. Res.,* **114,** D21205, doi:10.1029/2009JD012201.

——, K. P. Hamilton, Y. Wang, V. T. Phillips, and R. Bennartz, 2010: The impact of global warming on marine boundary layer clouds over the eastern Pacific—A regional model study. *J. Climate,* **23,** 5844–5863.

Lilly, D. K., 1968: Models of cloud-topped mixed layers under a strong inversion. *Quart. J. Roy. Meteor. Soc.,* **94,** 292–309.

Lin, J.-L., 2007: The double-ITCZ problem in IPCC AR4 coupled GCMs: Ocean–atmosphere feedback analysis. *J. Climate,* **20,** 4497–4525.

Lin, W. Y., M. H. Zhang, and N. G. Loeb, 2009: Seasonal variation of the physical properties of marine boundary layer clouds off the California coast. *J. Climate,* **22,** 2624–2638.

Lock, A. P., 2009: Factors influencing cloud area at the capping inversion for shallow cumulus clouds. *Quart. J. Roy. Meteor. Soc.,* **135,** 941–952.

Ma, C. C., C. R. Mechoso, A. W. Robertson, and A. Arakawa, 1996: Peruvian stratus clouds and the tropical Pacific circulation: A coupled ocean–atmosphere GCM study. *J. Climate,* **9,** 1635–1645.

Mansbach, D. K., and J. R. Norris, 2007: Low-level cloud variability over the equatorial cold tongue in observations and models. *J. Climate,* **20,** 1555–1570.

McCaa, J. R., and C. S. Bretherton, 2004: A new parameterization for shallow cumulus convection and its application to marine subtropical cloud-topped boundary layers. Part II: Regional simulations of marine boundary layer clouds. *Mon. Wea. Rev.,* **132,** 883–896.

Moeng, C. H., 2000: Entrainment rate, cloud fraction, and liquid water path of PBL stratocumulus clouds. *J. Atmos. Sci.,* **57,** 3627–3643.

Norris, J. R., and S. F. Iacobellis, 2005: North Pacific cloud feedbacks inferred from synoptic-scale dynamic and thermodynamic relationships. *J. Climate,* **18,** 4862–4878.

O'Dell, C. W., F. J. Wentz, and R. Bennartz, 2008: Cloud liquid water path from satellite-based passive microwave observations: A new climatology over the global oceans. *J. Climate,* **21,** 1721–1739.

Phillips, V. T. J., L. J. Donner, and S. T. Garner, 2007: Nucleation processes in deep convection simulated by a cloud-system-resolving model with double-moment bulk microphysics. *J. Atmos. Sci.,* **64,** 738–761.

——, P. J. DeMott, and C. Andronache, 2008: An empirical parameterization of heterogeneous ice nucleation for multiple chemical species of aerosol. *J. Atmos. Sci.,* **65,** 2757–2783.

——, and Coauthors, 2009: Potential impacts from biological aerosols on ensembles of continental clouds simulated numerically. *Biogeosciences,* **6,** 987–1014.

Pincus, R., M. Baker, and C. S. Bretherton, 1997: What controls stratocumulus radiative properties? Lagrangian observations of cloud evolution. *J. Atmos. Sci.,* **54,** 2215–2236.

Randall, D. A., J. A. Coakley Jr., C. W. Fairall, R. A. Kropfli, and D. H. Lenschow, 1984: Outlook for research on subtropical marine stratiform clouds. *Bull. Amer. Meteor. Soc.,* **65,** 1290–1301.

——, and Coauthors, 2007: Climate models and their evaluation. *Climate Change 2007: The Physical Science Basis,* S. Solomon et al., Eds., Cambridge University Press, 589–662.

Reynolds, R. W., T. M. Smith, C. Liu, D. B. Chelton, K. S. Casey, and M. S. Schlax, 2007: Daily high-resolution-blended analyses for sea surface temperature. *J. Climate,* **20,** 5473–5496.

Rossow, W. B., and R. A. Schiffer, 1999: Advances in understanding clouds from ISCCP. *Bull. Amer. Meteor. Soc.,* **80,** 2261–2287.

——, A. W. Walker, D. E. Beuschel, and M. D. Roiter, 1996: International Satellite Cloud Climatology Project (ISCCP) documentation of new cloud datasets. World Meteorological Organization Tech. Doc. WMO/TD 737, 115 pp.

Rozendaal, M. A., and W. B. Rossow, 2003: Characterizing some of the influences of the general circulation on subtropical marine boundary layer clouds. *J. Atmos. Sci.,* **60,** 711–728.

——, C. B. Leovy, and S. A. Klein, 1995: An observational study of diurnal variations of marine stratiform cloud. *J. Climate,* **8,** 1795–1809.

Sandu, I., B. Stevens, and R. Pincus, 2010: On the transitions in marine boundary layer cloudiness. *Atmos. Chem. Phys.,* **10,** 2377–2391.

Siebesma, A. P., and Coauthors, 2004: Cloud representation in general-circulation models over the northern Pacific Ocean: A EUROCS intercomparison study. *Quart. J. Roy. Meteor. Soc.,* **130,** 3245–3267.

Sun, Z., and L. Rikus, 1999: Improved application of exponential sum fitting transmissions to inhomogeneous atmosphere. *J. Geophys. Res.,* **104** (D6), 6291–6303.

Tiedtke, M., 1989: A comprehensive mass flux scheme for cumulus parameterization in large-scale models. *Mon. Wea. Rev.,* **117,** 1779–1800.

Wang, Y., 2001: An explicit simulation of tropical cyclones with a triply nested movable mesh primitive equation model—TCM3. Part I: Model description and control experiment. *Mon. Wea. Rev.,* **129,** 1370–1394.

——, O. L. Sen, and B. Wang, 2003: A highly resolved regional climate model (IPRC-RegCM) and its simulation of the 1998 severe precipitation event over China. Part I: Model description and verification of simulation. *J. Climate,* **16,** 1721–1738.

——, S.-P. Xie, H. Xu, and B. Wang, 2004a: Regional model simulations of marine boundary layer clouds over the southeast Pacific off South America. Part I: Control experiment. *Mon. Wea. Rev.,* **132,** 274–296.

——, H. Xu, and S.-P. Xie, 2004b: Regional model simulations of marine boundary layer clouds over the southeast Pacific off South America. Part II: Sensitivity experiments. *Mon. Wea. Rev.,* **132,** 2650–2668.

Wielicki, B. A., B. R. Barkstrom, E. F. Harrison, R. B. Lee III, G. L. Smith, and J. E. Cooper, 1996: Clouds and the Earth's Radiant Energy System (CERES): An Earth Observing System experiment. *Bull. Amer. Meteor. Soc.,* **77,** 853–868.

Winker, D. M., M. A. Vaughan, A. Omar, Y.-X. Hu, K. A. Powell, Z. Liu, W. H. Hunt, and S. A. Young, 2009: Overview of the CALIPSO mission and CALIOP data processing algorithms. *J. Atmos. Oceanic Technol.,* **26,** 2310–2323.

Wood, R., and C. S. Bretherton, 2004: Boundary layer depth, entrainment, and decoupling in the cloud-capped subtropical and tropical marine boundary layer. *J. Climate,* **17,** 3576–3588.

Wyant, M. C., C. S. Bretherton, H. A. Rand, and D. E. Stevens, 1997: Numerical simulations and a conceptual model of the stratocumulus to trade cumulus transition. *J. Atmos. Sci.,* **54,** 168–192.

——, and Coauthors, 2010: The PreVOCA experiment: Modeling the lower troposphere in the southeast Pacific. *Atmos. Chem. Phys.,* **10,** 4757–4774.

Xie, S.-P., 2004: The shape of continents, air-sea interaction, and the rising branch of the Hadley circulation. *The Hadley Circulation: Past, Present and Future,* H. F. Diaz and R. S. Bradley, Eds., Kluwer Academic Publishers, 121–152.

——, and Coauthors, 2007: A regional ocean–atmosphere model for eastern Pacific climate: Toward reducing tropical biases. *J. Climate,* **20,** 1504–1522.

Xu, H., S.-P. Xie, and Y. Wang, 2005: Subseasonal variability of the southeast Pacific stratus cloud deck. *J. Climate,* **18,** 131–142.

Xu, K. M., and D. A. Randall, 1996: A semiempirical cloudiness parameterization for use in climate models. *J. Atmos. Sci.,* **53,** 3084–3102.

Yu, L., and R. A. Weller, 2007: Objectively analyzed air–sea heat fluxes for the global ice-free oceans (1981–2005). *Bull. Amer. Meteor. Soc.,* **88,** 527–539.

Zhang, C., 2001: Double ITCZs. *J. Geophys. Res.,* **106** (D11), 11 785–11 792.

Zhang, M. H., and Coauthors, 2005: Comparing clouds and their seasonal variations in 10 atmospheric general circulation models with satellite measurements. *J. Geophys. Res.,* **110,** D15S02, doi:10.1029/2004JD005021.